remote sensing

MDPI

Article

Radiometric Retrieval of LWP and COD in Radiation Fog Using Dual-Height Observations, and the Observability of R_{eff}

Katarzyna Nurowska * and Krzysztof M. Markowicz

Institute of Geophysics, Faculty of Physics, University of Warsaw, 02-093 Warsaw, Poland; krzysztof.markowicz@fuw.edu.pl

* Correspondence: katarzyna.nurowska@fuw.edu.pl

Highlights

What are the main findings?

- A vertically separated two-station radiometer setup retrieves fog LWP and COD within an optimal estimation framework, evaluated against balloon soundings (PCC = 0.71, RMSE = 5.4 g m^{-2}); R_{eff} remains prior-dominated, an observability limit of broadband fluxes.
- Long-term data (224 episodes, 561 h) shows stable fog properties across seasons and years (median LWP $\approx$ 22 g m^{-2}, COD $\approx$ 3), with autumn dominance.

What are the implications of the main findings?

- This low-cost approach provides a practical alternative to microwave radiometers and cloud radars for continuous fog monitoring, especially in resource-limited regions.
- The retrieval saturates above LWP $\approx$ 30 g m^{-2}, defining a clear operational boundary for ground-based radiometric fog monitoring.

Abstract

A two-station radiometer configuration, vertically separated by 185 m, allows the retrieval of fog liquid water path (LWP) and cloud optical depth of fog (COD^f) within an optimal estimation framework coupled with the Fu–Liou radiative transfer model. LWP is the only reliably retrieved parameter, whereas the effective radius (R_{eff}) remains prior-dominated, because both broadband fluxes respond mainly to the LWP of the layer. A proof-of-concept evaluation against 28 tethered-balloon profiles from a three-day campaign gives a correlation of 0.71 and an RMSE of 5.4 g m^{-2} for LWP. The retrieval loses reliability for LWP $>$ 30 g m^{-2} where the radiative signal saturates. The long-term observations (2020–2025) comprise 224 fog episodes (561 h), with autumn dominating (99 episodes, 295 h). Seasonal median LWP ranges from 19.1 to 23.5 g m^{-2} (19.4–26.9 g m^{-2} with a fourfold weaker prior) and the mean COD^f stays near 3.1 $\pm$ 0.8, so the radiative impact of fog in the Strzyżów Valley is controlled by the frequency of fog rather than by the COD^f of individual events.

Keywords: radiation fog; microphysical properties; optimal estimation; radiative transfer; liquid water path; effective radius; cloud optical depth; fog optical depth; COD; LWP; R_{eff}

Check for updates

Academic Editor: Deaconu Lucia and Haipeng Zhang

Received: 21 July 2026
Revised: 16 September 2026
Accepted: 17 September 2026
Published: 24 September 2026

Copyright: © 2026 by the authors. Licensee MDPI, Basel, Switzerland. This article is an open access article distributed under the terms and conditions of the Creative Commons Attribution (CC BY) license.

1. Introduction

Fog develops in the planetary boundary layer (PBL) when interactions among radiative cooling, turbulent mixing, aerosols, and surface conditions promote the formation of

suspended droplets that significantly reduce visibility and interfere with transportation systems [1,2]. Climatologically, fog plays a crucial role in the surface radiation budget: it reflects incoming shortwave radiation during the day, causing surface cooling, while at night it traps outgoing longwave radiation and prevents the surface from cooling [2]. Understanding fog microphysical properties—particularly the effective radius (R_{eff}) and liquid water path (LWP)—is essential for accurate representation in numerical weather prediction (NWP) models and for assessing fog radiative impacts [3]. The need for such observational constraints is well documented: in an intercomparison of ten single-column and five large-eddy simulation models of a radiation fog case, only a minority of the participating single-column models reproduced the observed evolution of liquid water path, and operational forecasting centres continue to rank fog among their leading model deficiencies [4].

Obtaining reliable measurements of fog microphysical and optical properties remains difficult, particularly for thin fogs with low liquid water content. Lidar systems perform better in dense fog. For thin or near-surface fog layers, however, the backscatter signal is often too weak, and accurate retrievals are hindered by the near-range overlap issue, where the laser beam and the receiver field of view do not fully overlap. Conventional weather radars cannot detect fog-scale droplets (5–30 μm) because of the weak Rayleigh scattering. Satellite-based retrievals face similar challenges: passive infrared and microwave sensors typically have vertical resolutions exceeding 1 km, rendering them unable to resolve local fog layers.

Cloud radar can also be used to estimate fog liquid water content (LWC), not just LWP, with a vertical resolution of around 10 m [5]. Radar reflectivity is converted to LWC through a power-law relation whose pre-factor is not universal, so the synergy with a microwave radiometer is used to constrain it profile by profile [6]. Even with this synergy, vertical profiles of liquid water content inside fog remain scarce, which is one reason why numerical models still make the transition from optically thin to optically thick fog too abruptly [7]. The problem is that cloud radars are expensive and usually cannot measure below 40 m above ground, so the lowest part of the fog layer is not covered [5]. Dupont et al. [8] evaluated fog microphysical properties derived from in situ sensors, cloud radar, and the SYRSOC retrieval algorithm (algorithm calculating microphysical profiles from collocated data from cloud radar, ceilometer, and microwave radiometer), finding good agreement for droplet number concentration and R_{eff} profiles. However, a systematic overestimation of LWC was observed in the upper fog layer, since the algorithm was designed for clouds and does not fully capture the processes occurring within fog. An alternative to cloud-derived algorithms is the adiabatic fog framework of Toledo et al. [9], in which the fog liquid water path is linked to fog thickness through an equivalent adiabaticity. The associated liquid water path (LWP) decreases quasi-monotonously in the hour preceding dissipation and reaches a near-zero value at the fog life end.

The LWP of thin fogs (LWP $< 40\ \mathrm{g\,m^{-2}}$) is particularly important from a climatological perspective, as both longwave and shortwave surface radiative fluxes become sensitive to small changes in LWP and fog droplet size distribution [10]. Spectrally resolved measurements of downwelling longwave radiation using Atmospheric Emitted Radiance Interferometer (AERI) provide retrievals of fog particle effective radius and liquid water path once the fog visible optical depth exceeds about 0.25, below which the method loses sensitivity [11]. Recent advances in equipment miniaturisation [12] have made in situ measurements of fog microphysical properties possible using tethered balloons or unmanned aerial vehicles (UAVs), which allow examining the droplet size distribution with height as well as acquiring temperature and humidity profiles. However, such soundings are typically limited to short-term field campaigns and do not provide the temporal coverage

necessary to identify long-term variability or seasonal patterns. Such campaigns also show how variable the microphysics is: liquid water content, droplet number concentration and effective radius varied substantially both among the 42 fog events sampled at a single mid-latitude site and within individual events [13].

Microwave radiometers (MWRs) offer a complementary approach for continuous fog monitoring. An MWR is a passive remote sensing instrument that observes natural thermal emission from the atmosphere at microwave frequencies, typically within the K-band (20–30 GHz) and V-band (50–60 GHz) ranges. K-band frequencies are sensitive to water vapour and cloud liquid water, while V-band frequencies are sensitive to atmospheric temperature through oxygen absorption. Multi-frequency observations enable retrieval algorithms to reconstruct vertical profiles of temperature, humidity, and LWP [14]. MWRs are useful for fog studies because of their high temporal resolution (seconds to minutes) but they have some limitations. Recent assessments indicate that state-of-the-art passive microwave LWP retrievals have uncertainties of $\approx$20 g m^{-2}, while earlier work demonstrated that differences among microwave absorption models alone can produce systematic biases of about 15–30 g m^{-2} [15]. For thin fogs, this translates to large relative errors. Additionally, the maximum vertical resolution of boundary layer temperature profile retrievals from MWRs is approximately 50–200 m at the surface [16,17], which is insufficient to resolve the shallow surface-based temperature inversions that often precede radiation fog onset. Combining MWR measurements with infrared spectrometers can improve retrieval accuracy: neural network retrievals from this combined approach yield mean relative errors of 9% for LWP and 17% for R_{eff} [18]. Recent work by Guy et al. [19] demonstrated the utility of passive ground-based infrared spectroscopy for detecting fog onset and capturing microphysical evolution, which shows the potential of spectrally resolved measurements for fog studies.

Satellite remote sensing can provide information about fog on scales that are not possible to achieve with ground-based networks. The brightness temperature difference (BTD) method, exploiting the contrast between the 3.9 μm and 10.8 μm channels is one of the most established approaches for nighttime fog and low stratus detection [20]. During nighttime, the emission properties of fog at 3.9 μm differ measurably from those of clear-sky land surfaces, producing a characteristic signal that can be used to map fog extent. Cermak and Bendix [21] further refined this approach to improve discrimination of fog from elevated low stratus clouds, whose similar optical properties complicate remote detection.

Another common method for determining cloud properties uses look-up tables that compare satellite radiances with radiative transfer (RT) model simulations for different combinations of cloud parameters [22,23]. The simulation that matches the observations best gives the retrieved cloud properties. In the case of fog, satellite retrievals are more difficult because the observed radiances are strongly affected by surface emissions, and the thin vertical structures of fog layers violate the plane-parallel assumption that is usually used in radiative transfer inversions. Observations of fog and low-level clouds can nevertheless be performed using geostationary satellite data [24]. More broadly, satellite-based fog identification faces persistent limitations: discriminating radiation fog from low stratus remains difficult owing to their overlapping spectral signatures, surface emission interferes with retrievals over heterogeneous terrain, and the BTD method cannot be applied during daytime when reflected solar radiation dominates the 3.9 μm channel.

Machine learning (ML) methods have been used to improve satellite-based fog analysis. Nelli et al. [25] demonstrated that ML classifiers trained on multi-channel SEVIRI observations can detect fog more accurately than traditional BTD approaches over complex terrain. Cross-regional transferability was successfully demonstrated, though challenges remain for detecting fog patches with low optical thickness. Other approaches employ

machine learning trained on radiative transfer simulations to estimate LWP from geostationary SEVIRI observations, improving retrieval performance particularly for optically thin clouds. Satellite time series have also been used to study the full lifecycle of fog events, from onset through maturation to dissipation [24,26–28], and long-term satellite archives have enabled characterisation of spatial distributions and seasonal patterns of fog frequency on continental scales. For Poland specifically, station records document a long-term change in fog frequency and its variability [29]. Pauli et al. [28] produced a dataset describing fog and low stratus formation and dissipation times over large spatial and temporal scales, derived from geostationary imagery for central Europe. These studies provide valuable context for interpreting ground-based measurements, but they cannot deliver the microphysical detail—particularly R_{eff} and LWP—needed for radiation budget and NWP model evaluation.

One way to improve fog property retrievals is to use measurements at several vertical levels. Historically, cloud properties have been retrieved using ground-based and aircraft-mounted radiometers, such as in the Arctic Cloud Survey Project [30], though such measurements are expensive and limited to short observational periods. More commonly, ground-based and satellite measurements are used together for radiative closure studies to validate retrieval algorithms and assess data quality. For example, Dong et al. [31] performed a radiation closure study of single-layered, liquid-phase Arctic stratus clouds over the ARM North Slope of Alaska site, comparing cloud microphysical properties (optical thickness, LWP, R_{eff}) retrieved from CERES-MODIS imagery with ground-based ARM retrievals. Both sets of retrievals were used as inputs to the Fu–Liou radiative transfer model [32,33], and the simulated downwelling shortwave (SW) fluxes at the surface and upwelling shortwave fluxes at the top of the atmosphere agreed with the ARM and CERES flux observations to within 10 W m^{-2}. However, while radiative closure studies validate the mutual consistency of retrievals, measurements, and the radiative transfer model, they do not address the inverse problem of retrieving fog microphysical properties from radiation measurements alone.

The motivation for this study is that broadband radiative flux measurements at two vertically separated ground-based stations have not been used before for retrieving fog LWP, nor for testing to what extent they constrain R_{eff}. Broadband radiometers—such as pyranometers (for SW radiation) and pyrgeometers (for longwave radiation)—are widely deployed at meteorological and climate monitoring stations due to their relatively low cost, robustness, and ease of maintenance. Our configuration consists of two radiometers at different altitudes, one located above the fog layer, which gives information about the incoming fluxes, and a second one located at the bottom of the fog. This configuration provides information on the vertical gradient of radiative fluxes within fog, a quantity that is sensitive to both the amount and size distribution of fog droplets. This vertical gradient has not previously been leveraged for fog microphysical retrievals in the context of broadband radiation measurements.

This study presents the application of optimal estimation techniques [34] to retrieve fog LWP and cloud optical depth of fog (COD^{f}, given at the reference wavelength of 550 nm throughout this study), and to establish to what extent R_{eff} can be constrained, from broadband shortwave and longwave radiative flux measurements obtained at two vertically separated ground-based stations. The retrieval employs a Gauss–Newton iterative scheme combined with the Fu–Liou radiative transfer model [32,33] as the forward operator. Independent evaluation is performed using in situ measurements from a ShadowGraph instrument (at the ground) and OPC-N3 (mounted on the tethered balloon) during a fog field campaign in September 2023. Six years (2020–2025) of fog observations from Strzyżów, Poland, are analysed. This configuration offers a novel, cost-effective alternative

to expensive microwave radiometer or cloud radar systems, enabling continuous, long-term monitoring of fog microphysical properties. The retrieved fog properties facilitate characterisation of seasonal and inter-annual variability, enhancing understanding of fog climatology in the region and providing constraints for model evaluation.

2. Methods

Four kinds of observations are used in this study, each with a single, separate function. (i) The radiometers at the two stations (pyranometers and pyrgeometers, Section 2.1) provide the only input to the retrieval: the differences of downwelling shortwave and longwave fluxes between the stations are inverted with the optimal estimation scheme of Section 2.3.2 to retrieve LWP, COD^f and, by day, R_{eff}. (ii) The ground-based OPC-N3 at $SolarAOT_{lower}$, operating continuously since 2020, is used only to detect fog and to classify fog episodes (Section 2.5); its size distributions do not enter the retrieval. (iii) The in situ measurements of the field campaign of 9–11 September 2023 serve two purposes: the ground-based ShadowGraph provides the prior state and its covariance (Section 2.3.2), and the balloon-borne OPC-N3 provides the vertical profiles of LWC and R_{eff} against which the retrieval is evaluated (Section 3.3) as well as the width of the droplet size distribution assumed in the forward model. (iv) The camera at each station is used to verify the fog detection threshold and the position of the upper station relative to the cloud. The evaluation data and the prior thus come from the same campaign, which is why the sensitivity to the prior is examined separately in Section 3.3.1.

2.1. Measurement Sites

The retrieval was based on radiative flux measurements from two vertically separated stations. One station is situated below the fog—$SolarAOT_{lower}$ (at 260 m a.s.l., 49°52′18.0″N 21°48′26.0″E). $SolarAOT_{lower}$ is placed in Strzyżów city (a small town in southeastern Poland) on a slope of the valley. The second station—$SolarAOT^{upper}$—is located at the top of the hill in the Strzyżowskie foothills (at 445 m a.s.l., 49°52′43.0″N 21°51′40.8″E). The city lies next to the Wisłok River, and its position within a valley creates favourable conditions for fog formation. The geometry of the station pair has a horizontal distance of 4.06 km along an azimuth of 82° from $SolarAOT_{lower}$ to $SolarAOT^{upper}$, so that the station axis runs nearly west–east. The height difference between the stations is 185 m (levels in the model are at 0 and 185 m above the lower site, with the fog layer occupying 0–80 m).

2.2. Measurement Devices

2.2.1. $SolarAOT_{lower}$

The following instruments are mounted at the $SolarAOT_{lower}$ station:

- OPC-N3—optical particle counter, a low-cost aerosol particle counter capable of measuring particle number size distributions in the diameter range of approximately 0.35–40 µm. It allows calculation of the R_{eff}, which can be used to detect the presence of fog, as fog typically manifests as a distinct increase in the concentration of large droplets, reflected in elevated R_{eff} values. This device was used only for fog detection—comparing its results with the model is not possible since the instrument was not calibrated.
- CNR4 net radiometer for upward and downward SW and LW flux.
- Camera.
- HYT939—digital RH/temperature sensor.

During the field campaign during 9–11 September 2023 [35], there was a mobile laboratory equipped with an Aurora 4000 nephelometer, a Laser Aerosol Spectrometer LAS 3340A, and Oxford Lasers VisiSize D30 (ShadowGraph). At the $SolarAOT_{lower}$ station,

a tethered balloon was launched carrying the measurement setup, as described in the following subsection.

2.2.2. Balloon Apparatus

The balloon-based measurements were carried out using a compact payload comprising three primary sensors: (i) a GY-63 MS5611 high-performance pressure sensor module, (ii) a HYT939 temperature and relative humidity (RH) sensor, and (iii) an Alphasense OPC-N3 optical particle counter. The OPC-N3 measures particle size distributions across bins spanning 0.35–40 μm, along with mass concentrations of PM1.0, PM2.5, and PM10. Following the approach of [12], the OPC-N3 data were further processed to derive fog microphysical parameters, including LWC, effective droplet radius (R_{eff}), and droplet number concentration (N_c).

Sounding flights were launched at approximately 15 min intervals. During each flight, the balloon was allowed to ascend freely until the vertical ascent gave way to predominantly horizontal drift, at which point the balloon was retrieved. Vertical profiles obtained during the ascent and descent phases were averaged to produce a single representative profile per sounding. A detailed description of the measurement methodology is provided in [36].

2.2.3. SolarAOT$^{\mathrm{upper}}$

The SolarAOT$^{\mathrm{upper}}$ is a private radiative transfer research station (which collaborates with the University of Warsaw) located in an agricultural area. Several instruments are installed at the site, including a CMP21 pyranometer, an Eppley PIR pyrgeometer, a CIMEL sun photometer, an Aurora 4000 nephelometer, an AE-31 aethalometer, and a CHM-15K ceilometer.

Downwelling total (direct plus diffuse) SW (285–2800 nm) radiation was measured using a CMP21 Kipp & Zonen pyranometer. Complementary measurements of downwelling longwave (LW) radiation were obtained with an Eppley PIR pyrgeometer, which operates over the 4.5–50 μm spectral range. Both instruments were mounted on a levelled platform in an open, unobstructed location to ensure accurate radiative flux measurements.

A CIMEL sun–sky radiometer was used to measure direct and scattered solar radiation in nine spectral channels (340, 380, 440, 500, 675, 870, 936, 1020, and 1640 nm). Based on these measurements, the aerosol optical depth (AOD) and Ångström exponent were retrieved. The data are processed within the framework of the international AERONET program [37,38]. In this study, we used the data from the Aurora 4000 nephelometer, which measures aerosol scattering coefficients at three wavelengths (450, 525, and 630 nm) across 18 angular scattering sectors.

2.3. Model Setup and Configuration

Radiative transfer calculations were performed using the Fu–Liou radiative transfer model, a one-dimensional scheme originally developed by Fu and Liou [32,33]. The model computes shortwave and longwave radiative fluxes as well as atmospheric radiative heating rates, accounting for absorption, emission, and scattering by atmospheric gases, aerosols, and clouds. Gas-phase absorption is treated with the correlated *k*-distribution method, covering the primary absorbing constituents (H_2O, CO_2, O_3, CH_4, N_2O). The radiative transfer equation is solved using the δ-four-stream approximation, which provides an efficient compromise between accuracy and computational cost.

Cloud radiative effects are included by specifying cloud optical thickness, effective particle radius, phase (liquid water or ice), cloud top and base heights. Aerosol optical properties and their vertical distribution can likewise be prescribed. The model outputs upward and downward flux profiles, the net radiative budget at the surface and the top of the atmosphere (TOA), and vertical profiles of the atmospheric heating rate. This makes

the Fu–Liou scheme widely applicable to studies of cloud–aerosol–radiative interactions, satellite data validation, and radiative forcing analyses.

2.3.1. Input Data

For each fog case, two separate model simulations were performed—one for the SolarAOT$^{\text{upper}}$ (clear-sky/cloud above) and one for the SolarAOT$_{\text{lower}}$ (with the fog layer in between)—so that the radiative fluxes above and below the fog could be obtained. Both simulations are treated as a single run. In both cases, the height is measured relative to the lower station. The input profiles for the radiative transfer model are obtained by combining the 37 ERA5 [39] pressure levels, provided by the European Centre for Medium-Range Weather Forecasts (ECMWF), with a locally refined grid in the lowest kilometre.

The ERA5 vertical spacing (25 hPa, i.e., more than 200 m) is too coarse to resolve the fog layer, so additional levels are inserted there. The atmospheric pressure (p), temperature (T), and relative humidity (RH) values used as boundary conditions are based on the SolarAOT stations. For the lower-station case, the values of T and RH from SolarAOT$_{\text{lower}}$ (at 260 m a.s.l.) were interpolated in the first 80 m of the fog (with a resolution of 10 m) using the wet adiabatic lapse rate, and setting RH the same as at the ground. Between the fog top and the upper station, T and RH were interpolated linearly to the values measured at SolarAOT$^{\text{upper}}$ (445 m a.s.l.).

Above the station, additional levels were inserted every 50 m up to 1 km, with temperature and humidity interpolated from ERA5. The ERA5 levels range from 1000 hPa near the surface to 1 hPa in the stratosphere. Specifically, we extracted three-dimensional fields of p, T, and specific humidity (q) on 37 vertical model levels.

Above the refined grid, the standard ERA5 levels are used unchanged. The upper-station profile is constructed in the same way, but starts directly from the measured SolarAOT$^{\text{upper}}$ station values, without the fog layer. This yields about 60 levels for the lower-station and 56 for the upper-station profile. The exact number varies by one or two between cases, because the number of ERA5 levels lying above the top of the refined grid depends on the surface pressure of a given day.

Fog was parameterised as a homogeneous low-level liquid cloud layer of geometrical thickness dz (80 m). For the retrieval, we adopt a log-normal droplet distribution,

$$n(r) = \frac{N_c}{\sqrt{2\pi}\, r\, \sigma_{\ln}} \exp\left[-\frac{(\ln r - \ln r_g)^2}{2\sigma_{\ln}^2}\right], \tag{1}$$

where $n(r)$ is the droplet size distribution, r_g is the geometric-mean radius and $\sigma_{\ln} = \ln \sigma_g$ is the standard deviation of $\ln r$, with σ_g the geometric standard deviation. The R_{eff} is connected with r_g and $\sigma_{\ln}$ by the formula

$$R_{\text{eff}} = r_g \exp\left(\tfrac{5}{2}\sigma_{\ln}^2\right). \tag{2}$$

The geometric standard deviation is fixed at $\sigma_g = 1.88$ ($\sigma_{\ln} = 0.632$); the sensitivity of the retrieval to this assumption is quantified in Section 3.1. The value of σ was chosen based on our observations during the field campaign in Strzyżów in September 2023. We obtained the σ_g value from the Method-of-Moments fit to the in situ droplet spectra collected at Strzyżów with the balloon-borne OPC-N3 during the September 2023 campaign (averaged over all flights and all heights) during fog events. Values observed in other fog experiments have a similar magnitude, such as $\sigma_{\ln} = 0.262$ [40] or $\sigma_{\ln} = 0.405$ [41]. With this parameterisation the distribution retains a single free shape parameter (R_{eff}), while N_0 is scaled internally to match the target LWC.

Optical properties of fog (like extinction, SSA, g, and COD) were calculated using a dedicated Mie-based module for specified values of the droplet R_{eff} and LWP (assuming constant R_{eff} with height). These two parameters are the key unknowns retrieved in the optimisation procedure.

2.3.2. Optimal Estimation Retrieval of Fog Microphysical Properties

R_{eff} and LWP of the fog layer are retrieved using an optimal estimation (OE) approach [34], which combines prior knowledge of the state variables with radiative flux observations through a variational cost function.

The retrieval minimises the cost function:

$$J(\mathbf{x}) = (\mathbf{x} - \mathbf{x}_b)^{\mathrm{T}} \mathbf{B}^{-1} (\mathbf{x} - \mathbf{x}_b) + (\mathbf{y} - H(\mathbf{x}))^{\mathrm{T}} \mathbf{R}^{-1} (\mathbf{y} - H(\mathbf{x})) \quad (3)$$

where:

- $\mathbf{x} = [\text{LWP}, R_{\text{eff}}]^{\mathrm{T}}$ is the state vector, with LWP [g m^{-2}] and R_{eff} [µm];
- $\mathbf{x}_b$ is the a priori (background) state vector;
- $\mathbf{y} = [\Delta LW^{\downarrow}, \Delta SW^{\downarrow}]^{\mathrm{T}}$ is the observation vector, where $\Delta LW^{\downarrow} = LW^{\downarrow}(z_2) - LW^{\downarrow}(z_1)$ and $\Delta SW^{\downarrow} = SW^{\downarrow}(z_2) - SW^{\downarrow}(z_1)$ are the differences in downwelling longwave and shortwave fluxes between the SolarAOT$^{\text{upper}}$ station ($z_2 = 185$ m) and the surface station ($z_1 = 0$ m);
- $H(\mathbf{x})$ is the forward model operator—the Fu–Liou radiative transfer model that maps the state vector to the corresponding modelled flux differences;
- $\mathbf{B}$ is the background error covariance matrix;
- $\mathbf{R}$ is the observation error covariance matrix.

The first term in Equation (3) penalises departures from the a priori state, while the second term penalises mismatch between the modelled and observed radiation. At low solar elevation angles, the path length of sunlight through the atmosphere increases and surface reflections become highly geometry-dependent, leading to large and difficult-to-quantify uncertainties in the shortwave flux difference. To reduce this problem, we treat cases with solar elevation (el) below 10° as nighttime and cases above this threshold as daytime. For nighttime we use only the longwave observation, so $\mathbf{y}$ becomes a scalar and $\mathbf{R}$ a 1×1 matrix. For daytime cases, both longwave and shortwave fluxes are available, and the total $\mathbf{R}$ is assumed diagonal:

$$\mathbf{R} = \begin{pmatrix} \sigma^2_{\Delta LW} & 0 \\ 0 & \sigma^2_{\Delta SW} \end{pmatrix} \quad (4)$$

The diagonal elements of $\mathbf{R}$ represent the measurement uncertainties: $\sigma_{\Delta LW}$ combines the calibration uncertainties of the two pyrgeometers (longwave radiometers at z_1 and z_2), and $\sigma_{\Delta SW}$ combines those of the two pyranometers (shortwave radiometers).

Measurement uncertainties for each radiometer were estimated following instrument specifications (Table 1). For each radiation component, the total uncertainty was modelled as

$$\sigma = \sqrt{\sigma_0^2 + (\alpha \cdot F)^2}, \quad (5)$$

where σ_0 represents zero offsets and noise, α represents the fractional uncertainty due to calibration and directional response, and F is the measured flux (Table 1). Note that $\mathbf{R}$ varies with each observation, as the signal-dependent term makes the uncertainty a function of

the measured flux. The uncertainty of the flux difference between the SolarAOT^{upper} and SolarAOT$_{lower}$ stations was computed by quadrature propagation.

$$\sigma_{\Delta F} = \sqrt{\sigma_{upper}^2 + \sigma_{lower}^2} \tag{6}$$

The correlation between instruments mounted on SolarAOT^{upper} and SolarAOT$_{lower}$ was not taken into account as they are from different manufacturers, and there is a spatial separation between the sites. The manufacturer specifications used to derive $\sigma_{0,i}$ and α_i are quoted as worst-case (maximum) bounds for the Kipp & Zonen CMP21 [42] and CNR4 [43] instruments, with the explicit statement that "the performance specifications quoted are worst-case and/or maximum values" [44]. Following the recommendations of the WMO Guide to Instruments and Methods of Observation [45] and of the Guide to the Expression of Uncertainty in Measurement [46] (GUM, Section 4.3.7), the worst-case bounds are converted to 1σ Type B uncertainties under the assumption of a rectangular probability distribution:

$$u_{\mathrm{B}} = \frac{a}{\sqrt{3}}, \tag{7}$$

where a is the half-width of the stated bound.

The 4% temperature dependence of the CNR4 sensitivity given by the manufacturer refers to the full operating range (-10 $+40\,^{\circ}$C), but during the analysed fog episodes, the near-surface temperature varied only between -1.5 and $+15.9\,^{\circ}$C (5th–95th percentile). Since field intercomparisons of secondary-standard radiometers show sensitivities stable to within 1–2% under similar conditions [47,48], we reduce the temperature-dependence component to 1%—this originates from the thermal behaviour of the instrument housing so it affects both SW and LW channels equally. The remaining uncertainty components (calibration, non-linearity, zero offsets, window heating) are taken directly from the data sheet. Observation errors obtained this way are consistent with the retrieval residuals (median $\chi^2/m = 1.05$ for the two-channel daytime retrievals).

Table 1. Instrument error parameters used in the observation error covariance matrix **R**. For each radiometer, the spec value (from the cited document) and the corresponding 1σ value are reported. For the sensor mounted on the SolarAOT$_{lower}$, the CNR4 measuring LW radiation, daytime σ_0 includes the window-heating contribution, while nighttime drops the heating term. For the CNR4 SW lower sensor, the base term combines non-linearity, temperature dependence and stability. The values from the specification sheet are worst-case, and were transformed to 1σ based on [46] (GUM, Section 4.3.7).

	Multiplicative Uncertainty	**Zero-Offset**	
Instrument (Position, Spectral Range)	**α: spec $\rightarrow 1\sigma$**	**σ_0: spec $\rightarrow 1\sigma$ [W m^{-2}]**	**Reference**
Eppley PIR (SolarAOT^{upper}, LW)	0.01225 $\rightarrow$ 0.00707	2 $\rightarrow$ 1.15	[49]
K&Z CMP21 (SolarAOT^{upper}, SW)	0.0114 $\rightarrow$ 0.00659	9 $\rightarrow$ 5.20	[42]
K&Z CNR4 LW (SolarAOT$_{lower}$, LW), day	0.0173 $\rightarrow$ 0.01	7.21 $\rightarrow$ 4.16	[43]
K&Z CNR4 LW (SolarAOT$_{lower}$, LW), night	0.0173 $\rightarrow$ 0.01	4 $\rightarrow$ 2.31	[43]
K&Z CNR4 SW (SolarAOT$_{lower}$, SW), α_{base}	0.0173 $\rightarrow$ 0.01	15 $\rightarrow$ 8.66	[43]

The background error covariance matrix B was estimated from the in situ LWC and R_{eff} derived from the ShadowGraph observations at the surface station during the field campaign. LWP was derived by multiplying the in situ LWC by an assumed fog depth of 80 m.

$$\mathbf{B} = \begin{pmatrix} \sigma^2_{\mathrm{LWP}} & cov(\mathrm{LWP}, R_{\mathrm{eff}}) \\ cov(\mathrm{LWP}, R_{\mathrm{eff}}) & \sigma^2_{R_{\mathrm{eff}}} \end{pmatrix} = \begin{pmatrix} 10.72^2 & 12.96 \\ 12.96 & 1.92^2 \end{pmatrix} \tag{8}$$

The diagonal elements of **B** represent the assumed uncertainties of the a priori values: σ_{LWP} is the uncertainty of the a priori LWP [g m^{-2}], and $\sigma_{R_{\mathrm{eff}}}$ is the uncertainty of the a priori R_{eff} [µm]. The off-diagonal term 12.96 corresponds to a prior correlation $r_{\mathrm{LWP},R_{\mathrm{eff}}} = 0.63$. Larger values indicate weaker confidence in the prior, which allows the retrieval to move further away from $\mathbf{x}_b$. The elements not on the diagonal represent the covariance between a priori LWP and R_{eff}.

The a priori state was derived by averaging the in situ LWC and R_{eff} from all ShadowGraph observations taken during fog conditions: $\mathbf{x}_b$ = [19.17 10.79] (first element corresponds to LWP and second is R_{eff}). The method iteration is described in the Appendix A.

2.3.3. Fit-Quality Criteria

A retrieval was considered successful if the observation-space cost function J_{obs} fell below the 95th percentile of the χ^2 distribution

$$J_{\mathrm{obs}} = (\mathbf{y} - H(\hat{\mathbf{x}}))^{\mathrm{T}}\mathbf{R}^{-1}(\mathbf{y} - H(\hat{\mathbf{x}})) < \chi^2_{0.95,m}, \tag{9}$$

indicating that the difference between observations and the forward-model output at the analysed state was statistically consistent with the assumed error statistics. The m stands for how many observations were available, $m = 1$ for nighttime (LW only) and $m = 2$ for daytime (LW + SW), and $\hat{\mathbf{x}}$ is the retrieved (a posteriori) state. Cases exceeding this threshold are classified as bad-fit and excluded from the statistical analysis. Second, the full cost function including the background penalty term,

$$J = J_{\mathrm{obs}} + J_{\mathrm{prior}} = J_{\mathrm{obs}} + (\hat{\mathbf{x}} - \mathbf{x}_b)^{\mathrm{T}}\mathbf{B}^{-1}(\hat{\mathbf{x}} - \mathbf{x}_b), \tag{10}$$

was required to be below the 99th percentile of the χ^2 distribution with degrees of freedom equal to the number of observations ($J < \chi^2_{0.99,m}$). This additional check ensures that the solution is not only observationally consistent but also remains within a physically plausible region of the state space relative to the prior covariance.

To quantify how much information the observations contribute to the retrieval, we compute the degrees of freedom for signal (DFS). Following Rodgers' Rodgers [34] formalism, the DFS represents the number of independent pieces of information about the retrieved parameter that originate from the observations, as opposed to the a priori. Both quantities follow from the averaging kernel $\mathbf{A} = \mathbf{GK} = \partial\hat{\mathbf{x}}/\partial\mathbf{x}$, where $\mathbf{G} = \hat{\mathbf{S}}\mathbf{K}^{\mathrm{T}}\mathbf{R}^{-1}$ is the gain matrix (Equation (A8)): the retrieved state is $\hat{\mathbf{x}} = \mathbf{x}_b + \mathbf{A}(\mathbf{x} - \mathbf{x}_b) + \mathbf{G}\boldsymbol{\epsilon}$, where $\mathbf{x}$ is the true state and $\boldsymbol{\epsilon}$ the measurement error, so a diagonal element of **A** equal to 1 means that the observations fully determine that parameter, whereas a value of 0 means that the retrieval returns the prior. The DFS is the trace of **A**; with one observation at night and two by day, it cannot exceed 1 and 2, respectively. Throughout the paper, we report the LWP element of the diagonal as $\mathrm{DFS}_{\mathrm{LWP}}$, which at night is the whole DFS; for R_{eff} the corresponding element is close to zero in all daytime cases and is discussed in Section 3.3. The off-diagonal element $A_{\mathrm{LWP},R_{\mathrm{eff}}}$ describes how an error in the prior of R_{eff} propagates into the retrieved LWP.

2.3.4. Clear-Sky or Cloudy Conditions Above Fog

In this study, we use the difference between LW and SW fluxes above and below the fog layer. When the fog is thicker, the LW flux at the lower station gets closer to black-body emission and becomes less sensitive to conditions above the fog. On the other hand, correctly representing the atmospheric state above the fog is important for matching the model with observations at the upper station. Therefore, for each case, we compare the observed LW flux with a clear-sky model value at the upper level (above fog). If the

observation difference is larger than 10% from clear-sky conditions, an additional step is applied before the fog LWP and R_{eff} retrieval. A mid-level cloud layer 1 km thick centred at 600 hPa is added to the model, and its COD is adjusted to minimise the difference between the modelled and observed LW flux. Once the optimal COD is found, this cloud is retained in the model for the subsequent LWP and R_{eff} retrieval run. Because only the LW flux is minimised, this approach can be applied at night. For daytime cases with clouds above the fog, the two-parameter retrieval is therefore not attempted, and only LWP is retrieved from the longwave flux, as at night.

2.4. LWP and R_{eff} from Theoretical Study

The retrieved LWP values are compared with the LWP derived from the parameterisation of Stephens [50,51], which relates the cloud emissivity (ϵ_S) to the LWP through a mass absorption coefficient (a_0):

$$\epsilon_S(\mathrm{LWP}) = 1 - \exp\left(-a_0\,\mathrm{LWP}\right), \tag{11}$$

where a_0 is expressed in $\mathrm{m^2\,g^{-1}}$ and LWP in $\mathrm{g\,m^{-2}}$. The coefficient a_0 was obtained by Stephens [51] as a least-squares fit of Equation (11) to broadband emissivities computed with a multiple-scattering model for eight cloud types; for the downward flux, $a_0^{\downarrow} = 0.158\ \mathrm{m^2\,g^{-1}}$. For the downward longwave flux, Stephens [51] reports $a_0^{\downarrow} \approx 0.158\ \mathrm{m^2\,g^{-1}}$. This value corresponds to the broadband thermal-infrared range covered by broadband pyrgeometers, including the Eppley PIR (4–50 µm) and the Kipp & Zonen CNR4 (4.5–42 µm). For this reason, no spectral correction is applied to the measurements used in this study. The coefficient a_0 was originally derived by Stephens [51] for the modified gamma distribution of Deirmendjian [52] with R_{eff} from 3 to 10 µm.

In Stephens' work, the cloud base is assumed to emit as a grey body at temperature T_{cb}. The downward longwave flux measured above the fog, $LW_{\mathrm{up}}^{\downarrow}$, is taken as the clear-sky contribution transmitted through the cloud. Based on this assumption, the flux at the surface is

$$LW_{\mathrm{down}}^{\downarrow} = \epsilon_S(\mathrm{LWP})\,\sigma T_{cb}^4 + \left[1 - \epsilon_S(\mathrm{LWP})\right] LW_{\mathrm{up}}^{\downarrow}. \tag{12}$$

Solving Equation (12) for the emissivity and using Equation (11) yields

$$\epsilon_S = \frac{LW_{\mathrm{down}}^{\downarrow} - LW_{\mathrm{up}}^{\downarrow}}{\sigma T_{cb}^4 - LW_{\mathrm{up}}^{\downarrow}}, \qquad \mathrm{LWP} = -\frac{1}{a_0}\,\ln(1-\epsilon_S), \tag{13}$$

where the first expression is the emissivity derived from the two flux measurements and the second is the corresponding LWP. The formula saturates rapidly with increasing LWP. For LWP $\gtrsim$ 30 $\mathrm{g\,m^{-2}}$, the emissivity already exceeds 0.99, so the derived LWP loses sensitivity for optically thick fog.

A key finding of Stephens [51] is that the broadband longwave emissivity is nearly independent of the droplet distribution shape for a given LWP. The coefficient a_0 varies by only a few percent between narrow and broad distributions with the same LWP. In contrast, the shortwave $\mathrm{COD}_{SW} = \frac{3}{2}\,\mathrm{LWP}/(\rho_w\,R_{\mathrm{eff}})$ is inversely proportional to R_{eff} and depends strongly on the distribution [50]. This expression is derived under the geometric optics approximation, where the extinction efficiency factor $Q_{\mathrm{ext}} = 2$. This difference indicates that combining longwave and shortwave flux measurements in principle allows a simultaneous retrieval of LWP and R_{eff} under daytime conditions.

2.5. Fog Detection

Fog events were detected based on the R_{eff} derived from the size distributions of the ground-based OPC-N3 at $\mathrm{SolarAOT}_{\mathrm{lower}}$; this instrument serves only to detect fog and

plays no part in the retrieval. This device was not calibrated, so the size values may not correspond to the real particle sizes. However, the threshold selection is based only on the relative contrast between the fog and the background signal, which is not affected by the calibration. The detection threshold was set at R = 2.6 μm (10th bin of the OPC-N3), based on six years of OPC-N3 measurements. Outside the fog, the aerosol spectrum ends below 1 μm: in a typical sample, 95% of counts fall below 0.33 μm (median), and even for the 1% of the most coarse samples, the boundary does not exceed 0.85 μm. The intermediate range 1.5–2.6 μm is dominated by the hydrated aerosol and haze, and the fog signal there is comparable with the 99th percentile of the non-fog background (the ratio 0.8 for the 1.5–2.0 μm bin, 1.6 for the 2.0–2.6 μm bin), so a threshold based on these bins would confuse the fog with humid haze. Above R = 2.6 μm, the fog droplets start to dominate clearly: the median concentration in the fog exceeds the 99th percentile of the background by 2.3 times at 2.6–3.25 μm. The threshold 2.6 μm is a conservative choice—it may miss the earliest phase of the fog formation—but it guarantees that the detected events are fog, not the hydrated aerosol. The R_{eff} time series was smoothed using a 10 min running mean to reduce high-frequency noise.

A fog event was identified when R_{eff} exceeded the detection threshold for at least 25 out of 30 consecutive minutes. This approach accounts for potential short-term interruptions in the particle signal due to turbulence. A fixed detection threshold, defined as the 98.5th percentile of the smoothed R_{eff} distribution over the six-year measurement period (2020–2025), was then applied to obtain a binary fog presence indicator.

The choice of threshold was validated by manual inspection of concurrent camera imagery. For 20 randomly selected cases, the agreement between the algorithmically detected fog events and visual confirmation from the camera was 75% for the 98th percentile and 90% for the 98.5th percentile. Based on this validation, the 98.5th percentile was adopted as the detection threshold.

The final fog time series was sampled at 30 min intervals. Each data point represents whether fog was detected within a 30 min window centred on that timestamp. Due to this relatively long detection window, the method tends to miss rapid fog formation and dissipation phases, which in this region can occur on timescales of 15–30 min. Consequently, the dataset is biased towards persistent, fully developed fog events, and the timing of individual fog onsets and offsets may be uncertain by up to one sampling interval.

2.6. Temporal Sampling

All radiometric quantities at both stations are recorded every 36–44 s and the meteorological sensors every 1 min, and fog presence is evaluated from the 1 min OPC-N3 record at $\mathrm{SolarAOT}_{\mathrm{lower}}$ in 30 min windows as described above. The basic unit of the analysis is a case: a 30 min interval, centred on the half-hour timestamp, in which fog was detected. For each case the retrieval uses the downwelling fluxes and the temperature and humidity of both stations averaged over 10 min centred on the case timestamp (5 min on either side), after removal of outliers with a 10 min moving median. The 10 min window is a compromise: it is long enough to average the noise of the radiometer record, and short enough that the fluxes still correspond to the single solar geometry at which the forward model is evaluated. Around sunrise, the solar elevation changes by up to about 5° within 30 min, and the shortwave flux at $\mathrm{SolarAOT}^{\mathrm{upper}}$ then varies by 24–27 W m^{-2} (standard deviation of three consecutive 10 min means) within a 30 min window, so a 30 min average would mix radiative states that the model, run for one solar elevation, cannot represent; the fog itself also evolves on time scales of 15–30 min during formation and dissipation. Consecutive cases without interruption form one fog episode; a single 30 min interval without fog ends the episode. All long-term statistics in Section 4.2.2 and the episode dura-

tions, counts and total fog time (561 h) are therefore built from 30 min cases, and episode durations are multiples of 30 min.

2.7. Case Selection: Upper Station Above the Fog Top

Fog is detected, and its radiative effect measured, only at $\mathrm{SolarAOT_{lower}}$; $\mathrm{SolarAOT^{upper}}$ contributes a single quantity, the downwelling flux above the fog, which serves as the fog-free reference in the observation vector $\mathbf{y} = [\, LW^{\downarrow}_{185} - LW^{\downarrow}_{0};\ SW^{\downarrow}_{185} - SW^{\downarrow}_{0} \,]$. The homogeneity required over the 4 km separation is therefore that of the atmosphere above the fog top, i.e., of the thermodynamic profile of the boundary layer above the inversion and of any overlying cloud, and not that of the fog layer itself, which is a shallow, valley-confined feature. The optical depth of an overlying cloud is fitted for every case from the longwave flux measured at $\mathrm{SolarAOT^{upper}}$ and is then applied above $\mathrm{SolarAOT_{lower}}$, so that a horizontal difference in the overlying cloud between the two sites enters the retrieval as an error of the reference.

This construction fails only when $\mathrm{SolarAOT^{upper}}$ is itself inside a cloud, or inside a fog layer that extends above the altitude of the upper station. Such cases were identified by two conditions that had to hold simultaneously: a relative humidity above 95% measured at $\mathrm{SolarAOT^{upper}}$, and an effective sky emissivity above the fog top, $\epsilon_{\mathrm{top}} = LW^{\downarrow}_{185}/(\sigma T^4) > 0.95$, i.e., a sky radiating almost as a black body at the air temperature of the station. A total of 217 cases (30 min intervals, i.e., 108.5 h of fog), most of them in autumn and winter, met both conditions and were excluded from the analysis.

Each case is a 30 min interval; the fluxes entering the retrieval are 10 min averages centred on the case timestamp (Section 2.5). The wind measured above the fog at $\mathrm{SolarAOT^{upper}}$ is weak in the 770 accepted cases (median 2.5 $\mathrm{m\,s^{-1}}$, 10th–90th percentile 1.4–3.7 $\mathrm{m\,s^{-1}}$, never above 6 $\mathrm{m\,s^{-1}}$), so that the time needed for air to travel between the two sites has a median of 27 min, comparable to the length of a case. Averaging the fluxes over 30 min instead of 10 min changes the retrieved LWP by a median of 0.7 $\mathrm{g\,m^{-2}}$ (90th percentile 3.0 $\mathrm{g\,m^{-2}}$), well below the posterior uncertainty of the retrieval (median 6.3 $\mathrm{g\,m^{-2}}$), and only 2.5% of the 770 cases exceed that uncertainty. The variability of the longwave flux difference within the 30 min window, which, at the observed wind speeds, corresponds to a horizontal scale of about 4 km, is 2.0 $\mathrm{W\,m^{-2}}$ in the median, i.e., 40% of the measurement error assumed in $\mathbf{R}$, and propagates to 1.7 $\mathrm{g\,m^{-2}}$ of LWP.

3. Retrieval of Microphysical Properties

3.1. Sensitivity Study

This section presents the sensitivity to LWP and R_{eff} (assuming the 80 m layer depth of fog). This choice of fog height is consistent with the radiation-fog top heights observed at Strzyżów with the tethered-balloon profiles (Section 3.2). However, first, we checked how the depth of fog affects the retrieved value of LWP. A sensitivity test with pseudo-observations for an 80 m fog layer (LWP = 26.9 $\mathrm{g\,m^{-2}}$) was performed with the assumed depth varied between 50 and 200 m. Changing the assumed fog depth over the entire tested range affects the retrieved LWP by less than 11.5% (corresponding to a maximum error of 3.0 $\mathrm{g\,m^{-2}}$ for fog LWP = 26.9 $\mathrm{g\,m^{-2}}$). It can be seen that LWP, in contrast to LWC, is only weakly dependent on the assumed layer depth—the broadband radiances are mainly sensitive to the total amount of water in the layer rather than to how it is distributed vertically.

The retrieval assumes a vertically homogeneous fog layer. To quantify how much this assumption alone affects the retrieved quantities, we performed a synthetic experiment over a full grid of 45 cases (5 solar elevations × 3 values of LWP × 3 values of R_{eff}). In each case, six vertical profiles with identical LWP and identical height-averaged effective

radius were considered: a homogeneous control (S0), two profiles with a vertically varying liquid water content (S1, S2) and three profiles with a vertically varying effective radius (S3–S5). The effect of the vertical structure is calculated by comparing each profile with the homogeneous control of the same case.

Relative to the control, the profiles with a vertically varying liquid water content change the retrieved LWP by at most 0.1 g m^{-2} (0.5%); the profiles with a vertically varying effective radius change it by at most 0.28 g m^{-2} (1.8%) at night and 0.85 g m^{-2} (3.5%) during the day, well below the posterior uncertainty of the retrieval (1.4–9 g m^{-2}, depending on the case). The retrieved effective radius is prior-dominated and shows only negligible sensitivity to the vertical structure (at most 0.05 µm with respect to the control). The mechanism is the following: for vertically varying R_{eff} at fixed LWP and fixed mean R_{eff} the the COD^{f} of the layer is larger than that of the corresponding homogeneous layer because COD^{f} depends approximately on the vertical mean of $1/R_{\mathrm{eff}}$, i.e., on the harmonic rather than the arithmetic mean of R_{eff}. For the profiles considered here, this results in a 3–5% increase in optical depth. Because R_{eff} is prior-dominated in the homogeneous retrieval, the retrieval primarily attributes this increase in optical depth to LWP.

The only exception is the extreme case R_{eff} = 5 µm, in which the prescribed ±3 µm variation reaches the lower end of the droplet size range (2 µm) and the layer optical depth changes by 17–21% with respect to the homogeneous layer of the same LWP. There, the retrieved LWP changes by up to 2.8 g m^{-2} (18%) during the day, and the retrieved effective radius by up to 0.6 µm. This case is retained here as an upper bound.

The same synthetic framework was used to test the fixed width of the droplet size distribution. Pseudo-observations were generated for a homogeneous 80 m fog layer with LWP = 16 g m^{-2} and R_{eff} = 10.8 µm and a geometric standard deviation σ_g between 1.30 and 2.30, and were inverted with the operational operator, in which σ_g = 1.88 is fixed; all differences are taken with respect to the control run at the same LWP and R_{eff}, so that the prior offset cancels. A narrower distribution increases the downwelling longwave flux at the surface (by 2.1 W m^{-2} at σ_g = 1.30) and is interpreted by the retrieval as a larger LWP. Over this range, the retrieved LWP changes by at most 1.4 g m^{-2} (9%) at night and 0.8 g m^{-2} (5%) during the day, and R_{eff} by 0.2 µm; within the range fitted to the in situ spectra (σ_g = 1.64–1.92), the effect is below 0.6 g m^{-2} (4%) for LWP and 0.1 µm for R_{eff}, well inside the posterior uncertainties of 3.5–4.2 g m^{-2} and 1.7 µm.

Figure 1 presents the sensitivity of SW and LW radiation to changes of R_{eff} (left column) and LWP (right column) in an 80 m deep layer of fog. In fog conditions, LWC was ranging from 0.1 to 0.3 g m^{-3}. The graphs are drawn for LWC = 0.1/0.2/0.3, corresponding to LWP = 8/16/24 g m^{-2}, respectively. As can be seen from the right column of Figure 1, the LW fluxes are most sensitive to changes in droplet size within this LWP range.

Additionally, ΔLW and ΔSW depend on R_{eff} and LWP in different ways (compare the spread of the lines along the two vertical axes), so the joint measurement of ΔLW and ΔSW provides two constraints on the two unknowns and both R_{eff} and LWP can in principle be retrieved by minimising the cost function. The two constraints are, however, far from independent: both fluxes respond mainly to the COD^{f} of the layer, which is proportional to LWP$/R_{\mathrm{eff}}$, so an increase of R_{eff} produces almost the same pattern of ΔLW and ΔSW as a decrease of LWP. The small difference between the two patterns is what carries the information on R_{eff}, and Section 3.3 shows that it lies below the measurement uncertainty of the radiometers. For the typical LWP range of fog at our site (LWP between 8 and 40 g m^{-2}), $|\Delta LW|$ is approximately 20–80 W m^{-2}, and $|\Delta SW|$ for $\theta \geq 10^{\circ}$ is approximately 100–250 W m^{-2}. Both values are well above the calibration uncertainty of the radiometers (Table 1).

However, at night and for low solar elevation, the downwelling SW signal is zero or drops to the instrument noise level (top three rows of the Figure 1, corresponding to $\theta \leq 10°$), so ΔSW no longer carries useful information about the fog microphysics. In this case, only ΔLW remains informative, and a single observable can constrain only a single parameter. For this reason, the retrieval is split according to solar elevation: for $\theta < 10°$ (nighttime and low-sun conditions), a one-dimensional retrieval of LWP is performed, with R_{eff} held fixed at its a priori value; for $\theta \geq 10°$, the full two-dimensional retrieval of both LWP and R_{eff} is performed. The 10° threshold corresponds to the lowest elevation at which ΔSW becomes detectable above the calibration uncertainty of the SW radiometers in our setup.

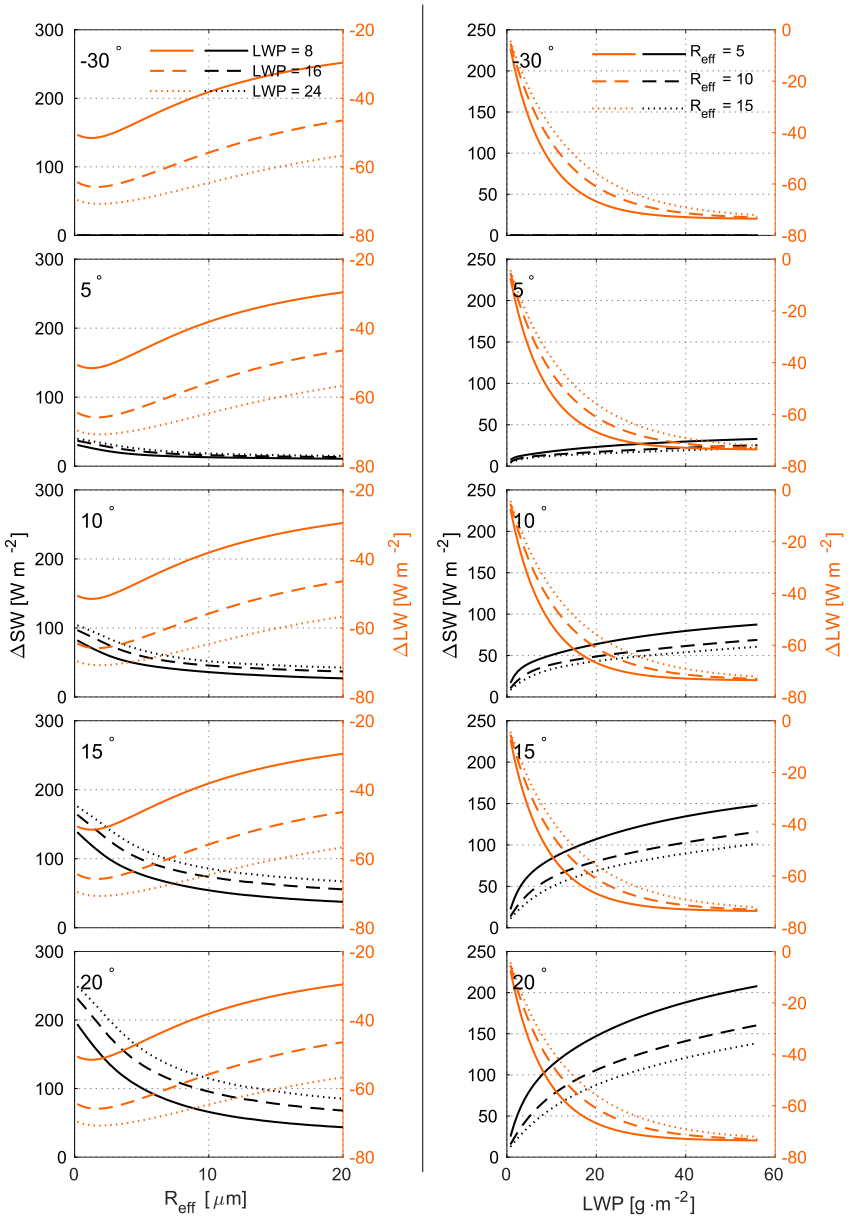


Figure 1. Sensitivity of SW (left vertical axis, black lines, different line style) radiative flux or LW (right vertical axis, orange lines, different line style) to changes of R_{eff} (left column) or LWP (right column) for a given sun elevation angle: $-30°$, $5°$, $10°$, $15°$, $20°$ (consecutive rows). The modelled fog extended from ground level to 80 m. Δ stands for the difference in SW/LW radiation between 185 m above ground (conditions above fog) and on the ground (below the fog).

The term $LW^{\downarrow}_{\text{down}}$ and $SW^{\downarrow}_{\text{down}}$ refers to radiation at $\text{SolarAOT}_{\text{lower}}$ and $LW^{\downarrow}_{\text{up}}$ or $SW^{\downarrow}_{\text{up}}$ refers to radiation at $\text{SolarAOT}^{\text{upper}}$ (the height difference between the stations is 185 m).

The left column of Figure 1 shows that for a fixed LWP, an increase in droplet size reduces the magnitude of both ΔSW and ΔLW. The two quantities have opposite signs. The SW radiation is attenuated as it propagates downward through the fog layer, so $SW^{\downarrow}_{\mathrm{up}} > SW^{\downarrow}_{\mathrm{down}}$ and $\Delta SW > 0$.

The downwelling LW radiation, in contrast, is enhanced at the ground, because the fog emits at the near-surface temperature with a high emissivity (ϵ = 0.7–0.95 for the typical LWP range of our sample), so $LW^{\downarrow}_{\mathrm{down}} > LW^{\downarrow}_{\mathrm{up}}$ and $\Delta LW < 0$. It is the remaining departure of ϵ from unity that carries the LWP information exploited by the retrieval; once the emissivity saturates (LWP $\geq 30\ \mathrm{g\,m^{-2}}$, COD ≈ 4.4)—see Table 2—this sensitivity is lost. The decrease of $|\Delta SW|$ with droplet size follows from Mie theory: larger droplets scatter more strongly in the forward direction, so a larger fraction of the incoming SW radiation reaches the ground. The decrease of $|\Delta LW|$ has the same microphysical origin. For a fixed LWP, an increase in R_{eff} reduces the COD. The fog becomes more transparent in the LW window, $LW^{\downarrow}_{\mathrm{down}}$ approaches $LW^{\downarrow}_{\mathrm{up}}$, and ΔLW approaches zero from below.

Table 2. Longwave emissivity, $\epsilon = 1 - e^{-\mathrm{COD}}$, as a function of COD and corresponding LWP for the assumed fog in the simulations.

LWP [g m^{-2}]	COD	ϵ
8	1.16	0.685
16	2.31	0.901
24	3.47	0.969
30	4.39	0.988
36	5.20	0.995
40	5.78	0.997

3.2. Independent Evaluation of the Model

During 9–11 September 2023, a field campaign focused on fog measurements was conducted at the SolarAOT$_{\mathrm{lower}}$ station; the campaign data are published in Nurowska [35]. Fog events were observed each night during this period. Apart from ShadowGraph measurement on the ground, balloon soundings were performed during the campaign to derive LWP and R_{eff} in the fog from the size distributions of the balloon-borne OPC-N3. The mean depth of fog was 83 m (not taking into account fogs that were less than 50 m thick). Simulations of fog conditions appearing on 9–11 September 2023 were performed to evaluate the model. The measured T and RH profiles, together with the in situ LWC and mean R_{eff} derived from the balloon-borne OPC-N3 for each flight, were used. The modelled LW and SW radiation at SolarAOT$^{\mathrm{upper}}$ and SolarAOT$_{\mathrm{lower}}$ stations was compared with the observations. The results are provided in Figure 2, in which the left panel presents the SW and the right panel the LW radiation. The upper row presents the values at the SolarAOT$^{\mathrm{upper}}$ station, the middle row those at the SolarAOT$_{\mathrm{lower}}$ station, and the lower row the difference between the SolarAOT$^{\mathrm{upper}}$ and SolarAOT$_{\mathrm{lower}}$ stations.

Overall, the model reproduces SW fluxes well in all three panels: regression slopes range from 0.91 to 1.02 and biases remain within $\pm 5.1\ \mathrm{W\,m^{-2}}$. The SW upper and lower panels both show tight clustering around the 1:1 line (RMSE $\approx$ 14–18 $\mathrm{W\,m^{-2}}$), confirming that the model reproduces the attenuation of shortwave radiation through the fog layer realistically. The ΔSW panel exhibits slightly larger scatter (RMSE = 18.3 $\mathrm{W\,m^{-2}}$, bias = $-4.8\ \mathrm{W\,m^{-2}}$), likely due to the assumption of a height-independent droplet size distribution characterised by only one parameter, R_{eff}.

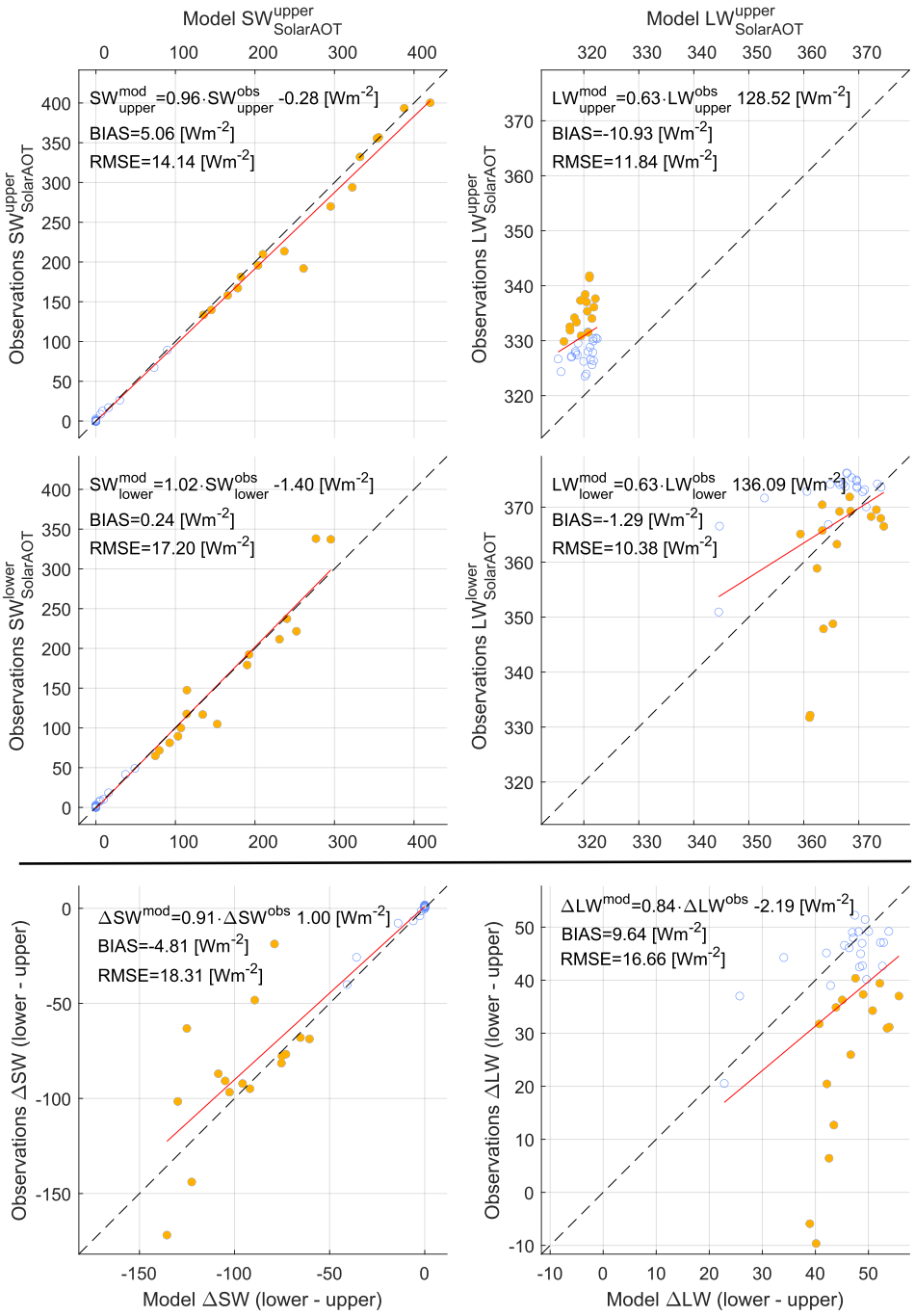


Figure 2. Scatter plots comparing modelled (horizontal axes) versus observed (vertical axes) radiative fluxes for the three fog events (9–11 September 2023). Left column: SW fluxes; right column: LW fluxes. Rows show fluxes from $\mathrm{SolarAOT}^{\mathrm{upper}}$ (above the fog layer; top row), from $\mathrm{SolarAOT}_{\mathrm{lower}}$ (below the fog layer; middle row), and the fog-layer difference, $\Delta = \mathrm{SolarAOT}_{\mathrm{lower}} - \mathrm{SolarAOT}^{\mathrm{upper}}$ (bottom row). Orange filled circles represent day events ($\theta \geq 10°$), while blue open circles represent night events. The black dashed line indicates the 1:1 line; the red solid line is the linear regression fit.

The LW fluxes are less well reproduced. Both LW above and below fog panels show compressed regression slopes of ≈0.63, indicating that the model underestimates the full range of observed variability. The LW upper panel displays the largest negative bias ($-10.9\ \mathrm{W\,m^{-2}}$), suggesting a systematic underestimation of downward longwave radiation above the fog layer, which is often related to the model not representing the temperature profiles in the upper boundary layer well enough. The LW lower panel shows markedly improved agreement (bias = $-1.3\ \mathrm{W\,m^{-2}}$, RMSE = $10.4\ \mathrm{W\,m^{-2}}$), with data points distributed

closer to the 1:1 line. The ΔLW panel reveals a positive bias of 9.6 W m^{-2} and RMSE of 16.7 W m^{-2}, meaning the model tends to overestimate the longwave flux difference across the fog layer.

The yellow points in the ΔLW plot that deviate significantly from the 1:1 line correspond to the moments of fog dissipation (observations after 6 UTC), when the fog had a patchy structure—which was not reflected in the model. Night fog points (blue circles) are mostly at the edges of each panel and generally closer to the 1:1 line compared to day fog points, which suggests the model works better for nighttime fog.

3.3. Independent Evaluation of the Retrieval

The model, configured as described in Section 2.3, was run for the field campaign period. The 2D optimal estimation retrieval simultaneously retrieves LWP (for night and day) and R_{eff} (for day—observations when the sun elevation is above $\theta \geq 10^{\circ}$) from ground-based broadband radiative flux differences. A total of 38 retrieval cases were processed from the balloon-based radiative flux measurements, and 34 were classified with cost function below χ^2 (0.95, nr of observations). Cases were split into 12 daytime cases (solar elevation $\geq 10^{\circ}$), where LWP and R_{eff} were retrieved together from both LW and SW fluxes, and 22 nighttime cases ($el < 10^{\circ}$), where only LWP was retrieved from the LW flux.

To evaluate the retrieved parameters against independent measurements, we compare the retrieval results with the profiles from the balloon-borne OPC-N3 (Section 2.2.2), which are independent of both the retrieval and the fog detection (Figure 3). For LWP, the 28 cases show good agreement (PCC = 0.71, RMSE = 5.4 g m^{-2}, bias = -2.2 g m^{-2}), with a regression slope close to unity ($y = 0.94x + 3.40$). Six cases with LWP > 30 g m^{-2} are shown on the plot but excluded from the best-fit line, as we find the retrieval becomes unreliable above this threshold: the radiative signal saturates and the flux difference no longer scales with increasing liquid water content. Four cases are marked as rejected due to a too large cost function. For R_{eff}, the agreement is significantly weaker (PCC = 0.17, RMSE = 2.03 µm, bias = 1.90 µm), with a slope ($y = 1.62x + 1.54$) and a systematic positive bias. This comparison should be read as a consistency check rather than as a validation: the retrieved R_{eff} does not depart from the prior (Section 4.2.1), so the agreement with the balloon data reflects the closeness of the prior to the in situ droplet sizes, not information extracted from the fluxes.

A common prior of $\langle x_b \rangle = 19.2$ g m^{-2} was used for all nighttime cases. The mean analysed LWP across all night cases is $\langle \text{LWP}_a \rangle = 21.4 \pm 5.1$ g m^{-2}. The DFS [34] averages 0.728 ± 0.129 (range 0.447–0.982, maximum possible 1), indicating that the LW observations carry a moderate but consistent amount of independent information about LWP (values closer to unity imply that the observation adds significant information to the prior, while values approaching zero would indicate a prior-dominated retrieval).

The quality of the fit is assessed through the observation-space residuals, $\mathbf{y} - H(\mathbf{x})$. Before retrieval (prior model minus observations), the residual mean and standard deviation are -2.1 ± 8.6 W m^{-2} (RMSE = 8.6 W m^{-2}), corresponding to RMSE/$\sigma_R = 1.7$ (with assumed $\sigma_R = 5.1$ W m^{-2}). After retrieval, residuals tighten to -1.1 ± 1.4 W m^{-2} (RMSE = 1.8 W m^{-2}, RMSE/$\sigma_R = 0.35$). The reduction of the RMSE to well below the assumed observation noise level (RMSE/$\sigma_R < 1$) confirms that the forward model, given the retrieved parameters, reproduces the observed fluxes within measurement uncertainty.

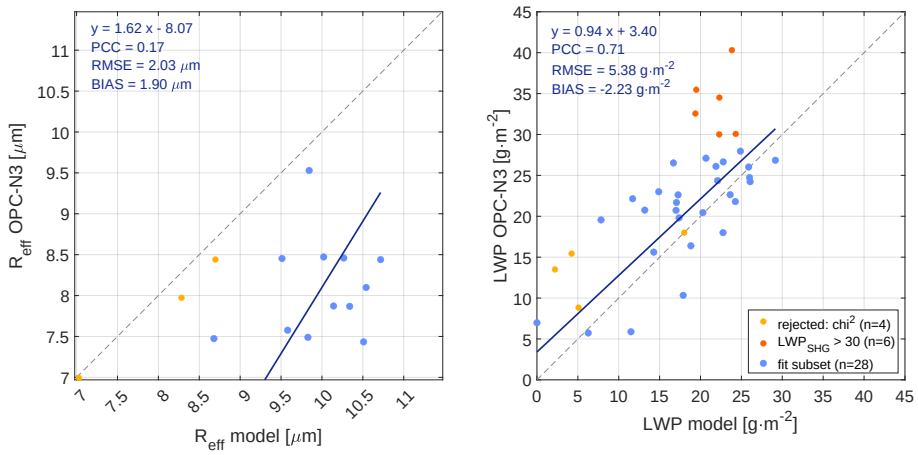


Figure 3. Scatter plot comparing model-retrieved values of R_{eff} (**left** panel) and LWP (**right** panel) against LWP and R_{eff} derived from the balloon-borne OPC-N3. Points are colour-coded as follows: yellow—rejected as they did not pass the χ^2 test; orange—balloon-derived LWP exceeds 30 g m^{-2} (excluded from the total least square regression); blue—good (not rejected) cases. The solid blue line shows the total least square regression line; the grey dotted line represents 1:1 proportionality. PCC denotes the Pearson correlation coefficient and RMSE the root mean square error.

For daytime observations, both LW and SW fluxes are available. Therefore, we attempted to retrieve two unknown parameters LWP and R_{eff}. The prior values are LWP = 19.2 g m^{-2} and $R_{\text{eff}} = 10.79$ µm. The analysed means are $\langle \text{LWP}_a \rangle = 15.7 \pm 3.9$ g m^{-2} and $\langle R_{\text{eff},a} \rangle = 10.12 \pm 0.40$ µm. The total DFS is 0.891 ± 0.108 (range 0.642–1.016, maximum possible 2), of which about 0.9 is attributable to LWP and close to zero to R_{eff}: the two-height broadband fluxes add essentially no information on R_{eff} beyond the prior.

After retrieval, both residuals decrease relative to the prior: RMSE_{LW} drops from 11.0 to 5.8 W m^{-2} ($\sigma_R = 6.2$ W m^{-2}; RMSE/σ_R from 1.8 to 1.0) and RMSE_{SW} from 14.3 to 13.2 W m^{-2} ($\sigma_R = 10.3$ W m^{-2}; RMSE/σ_R from 1.4 to 1.3). The LW residual thus falls below the assumed observation noise, while the SW residual remains marginally above it, reflecting a small systematic SW offset (mean +10.8 W m^{-2}); overall, the retrieval meaningfully reduces the model–observation mismatch in both channels.

The retrieval system reproduces the observed radiative fluxes for both nighttime and daytime fog cases close to the measurement uncertainty (post-retrieval $\text{RMSE}/\sigma_R = 0.35$ at night, and 0.95 for LW/1.29 for SW during the day). LWP is the dominant constrained parameter ($\text{DFS}_{\text{LWP}} \gtrsim 0.7$ in both configurations).

3.3.1. Sensitivity to the Prior

All statistics in this and the following subsection refer to the 770 accepted cases, i.e., the retrievals passing the fit-quality criteria of Section 4.2.1 after the exclusion of the cases with the upper station inside the cloud (Section 2.7). Because the prior state $\mathbf{x}_b$ comes from the same ShadowGraph campaign that also provides the in situ evaluation data, we quantified how much of the retrieved LWP is inherited from it. The sensitivity was evaluated in the local linear approximation around each converged solution, using the Jacobian $\mathbf{K}$, the observation covariance $\mathbf{R}$ and the prior covariance $\mathbf{B}$ stored for every case, so that no re-run of the radiative transfer model was needed; the procedure and its validation against the full non-linear retrieval are given in Appendix D. We shifted the prior mean of LWP by ±25% and ±50%, the prior mean of R_{eff} by ±25%, and widened the prior covariance by factors of 2, 4 and 10 (Table 3).

A ±25% change of the prior LWP mean (4.8 g m^{-2}) moves the median retrieved LWP by 1.6 g m^{-2} (7.2% of the median) and ±50% by 3.1 g m^{-2} (14.3%), the median transfer

coefficient $1 - A_{\mathrm{LWP}}$ being 0.34 at night and 0.13 by day. Because $\sigma_{\mathrm{post}} = \sigma_b\sqrt{1-A}$ in the one-dimensional case while the induced shift is $(1-A)\,|\Delta\mathbf{x}_b|$, no case exceeds its posterior uncertainty. The coefficient is not uniform: A_{LWP} is 0.8–0.9 below 20 g m^{-2} and 0.4–0.5 above it, where the longwave signal saturates. Weakening the prior barely changes the level: with $\mathbf{B}' = 4\mathbf{B}$, the median moves by $+1.1$ g m^{-2} although DFS rises from 0.67 to 0.89 and the 10th–90th percentile range widens from 14.8–28.2 to 14.3–33.9 g m^{-2}. The level near 22 g m^{-2} is therefore set by the observations, consistent with the prior-minus-observation residual of -2.1 ± 8.6 W m^{-2} quoted above; the prior does, however, compress the seasonal contrast: with $\mathbf{B}' = 4\mathbf{B}$, the spread between the highest and the lowest seasonal median grows from 4.4 to 7.5 g m^{-2} and the inter-annual spread from 5.6 to 8.5 g m^{-2} (Table 4). DJF is the most prior-dependent season (median sensitivity 0.63 g m^{-2} per g m^{-2} of prior shift, against 0.33 for the whole sample) and, with only 12 cases, is not interpreted seasonally. In the daytime 2D retrieval, R_{eff} follows its prior with a slope of 1.07 and a $\pm$25% change of that prior propagates into LWP as $\pm$3.5 g m^{-2} (18.5%), so daytime LWP inherits the R_{eff} prior uncertainty.

Table 3. Sensitivity of the retrieved LWP to the prior, evaluated in the local linear approximation described in Appendix D. Baseline prior: $\mathbf{x}_b = [19.2$ g m^{-2}, 10.8 µm$]$, $\sigma_{\mathrm{LWP}} = 10.7$ g m^{-2}. All entries are medians over the 770 cases; the last column is the fraction of cases in which the induced shift exceeds the posterior uncertainty of the unperturbed retrieval.

Prior Variant	LWP [g m^{-2}]	Shift [g m^{-2}] (% of Baseline Median)	$p_{90}\lvert\mathrm{Shift}\rvert$ [g m^{-2}]	DFS	σ_{post} [g m^{-2}]	$\lvert\mathrm{Shift}\rvert > \sigma_{\mathrm{post}}$ [%]
baseline	22.0	—	—	0.67	6.2	0.0
$\mathbf{x}_b^{\mathrm{LWP}} - 50\%$	18.2	−3.1 (−14.3)	6.6	0.67	6.2	0.0
$\mathbf{x}_b^{\mathrm{LWP}} - 25\%$	20.0	−1.6 (−7.2)	3.3	0.67	6.2	0.0
$\mathbf{x}_b^{\mathrm{LWP}} + 25\%$	24.1	+1.6 (+7.2)	3.3	0.67	6.2	0.0
$\mathbf{x}_b^{\mathrm{LWP}} + 50\%$	26.3	+3.1 (+14.3)	6.6	0.67	6.2	0.0
$\mathbf{B}' = 2\mathbf{B}$	22.7	+0.7 (+3.1)	3.3	0.80	6.9	0.0
$\mathbf{B}' = 4\mathbf{B}$	23.4	+1.1 (+5.1)	6.5	0.89	7.3	3.4
$\mathbf{B}' = 10\mathbf{B}$	23.8	+1.5 (+7.0)	9.6	0.95	7.7	15.3

Table 4. Median retrieved LWP [g m^{-2}] per season and per year for the baseline prior and for three prior variants; n is the number of cases. DJF is represented by only 12 cases after the exclusion described in Section 2.7 and is not interpreted seasonally.

	n	Baseline	$\mathbf{x}_b^{\mathrm{LWP}} - 25\%$	$\mathbf{x}_b^{\mathrm{LWP}} + 25\%$	$\mathbf{B}' = 4\mathbf{B}$
DJF	12	19.1	15.6	22.7	19.4
MAM	192	22.5	20.4	25.1	24.7
JJA	148	23.5	21.4	26.4	26.9
SON	418	21.1	19.4	22.9	21.9
2020	224	23.1	20.6	26.2	26.7
2021	191	20.2	19.1	21.2	20.3
2022	99	22.7	20.5	24.9	24.4
2023	130	20.1	18.5	21.7	20.7
2024	90	20.8	19.7	21.8	20.7
2025	36	25.7	24.0	27.6	28.8
all	770	22.0	20.0	24.1	23.4

3.3.2. Uncertainty Budget

Table 5 collects the individual contributions to the uncertainty of the retrieved LWP and R_{eff} quantified in this study, separated into the terms of the inverse problem, which are described by the covariances $\mathbf{R}$ and $\mathbf{B}$, and the assumptions of the forward model, which

are evaluated as bounds from the synthetic experiments. The posterior uncertainty of a single LWP retrieval (median 6.3 g m^{-2}) is dominated by the radiometric measurement error propagated through the gain matrix (4.7 g m^{-2}), with the prior constraint contributing 3.7 g m^{-2} in the median and up to 7.5 g m^{-2} for the cases with an overlying cloud. The systematic terms are smaller: a ±25% error in the prior mean moves a single retrieval by 1.6 g m^{-2} in the median, the assumed fog depth and vertical structure by at most 3.0 and 0.85 g m^{-2}, respectively, the assumed width of the droplet size distribution by 0.6 g m^{-2} within the range fitted to the in situ spectra (1.4 g m^{-2} over an extreme range), and the 4 km separation of the stations by 0.7 g m^{-2}. The empirical RMSE of 5.4 g m^{-2} against the tethered-balloon LWP is consistent with the posterior uncertainty, which indicates that the error model in **R** and **B** is realistic. For R_{eff} the budget shows the opposite balance: the measurement term is small (0.4 µm) and the posterior uncertainty (1.8 µm) remains close to the prior one (1.9 µm), so that the daytime R_{eff} is set by the prior and a ±25% error in that prior propagates almost fully into R_{eff} (2.9 µm) and adds 3.5 g m^{-2} to the daytime LWP.

Table 5. Uncertainty budget of the retrieved LWP and R_{eff}. The LWP column refers to the 770 accepted cases, the R_{eff} column to the 40 daytime cases in which R_{eff} is retrieved. In the upper block, the entries are the median over the cases and, in parentheses, the 90th percentile; where a single value is given, only the median was evaluated. Rows (1) and (2) add in quadrature to the posterior uncertainty, rows (3)–(5) are systematic shifts, and row (5) is largely contained in **R** and is not added again. In the lower block, the entries are upper bounds from the synthetic experiments; for row (8), the bound rises to 2.8 g m^{-2} and 0.6 µm in the extreme case R_{eff} = 5 µm, and for row (9) to 1.4 g m^{-2} and 0.2 µm over the extreme range σ_g = 1.30–2.30. Row (10) is the empirical total. n.e.: not evaluated.

	Source	LWP [g m^{-2}]	R_{eff} [µm]	Described in
Retrieval (inverse problem)				
(1)	Radiometric measurement error, $\mathbf{GRG}^{\mathrm{T}}$	4.7 (5.3)	0.38 (0.42)	Appendix A, Table 1
(2)	Prior constraint, $(\mathbf{I}-\mathbf{A})\mathbf{B}(\mathbf{I}-\mathbf{A})^{\mathrm{T}}$	3.7 (7.5)	1.74 (1.86)	Appendix A
	Posterior uncertainty σ_{post} = (1) ⊕ (2)	6.3 (8.9)	1.79 (1.88)	Appendix A
(3)	Prior mean of LWP changed by ±25%	1.6 (3.3)	0.3	Section 3.3.1, Appendix D
(4)	Prior mean of R_{eff} changed by ±25%	3.5 (5.6)	2.9 (2.9)	Section 3.3.1, Appendix D
(5)	Flux variability on the 4-km scale (30 min vs. 10 min averaging)	0.7 (3.0)	0.06 (0.24)	Section 2.7
Forward model (Fu–Liou, fog layer)				
(6)	Fog depth 50–200 m instead of 80 m	3.0	n.e.	Section 3.1
(7)	Vertical structure of LWC	0.1	0.05	Section 3.1
(8)	Vertical structure of R_{eff}	0.85	0.05	Section 3.1
(9)	Width of the droplet size distribution, σ_g = 1.64–1.92 instead of 1.88	0.6	0.1	Section 3.1
(10)	Independent evaluation against tethered-balloon data (RMSE, n = 28)	5.4	2.0	Section 3.3

4. Data Analysis

4.1. Fog Occurrence and Duration Statistics

Fog events at the SolarAOT$_{\mathrm{lower}}$ station were detected using the OPC-N3 based algorithm described in Section 2.5, where cases (30 min intervals with fog) and episodes (uninterrupted sequences of cases) are defined. Because radiative fogs mostly occur at night, we define a day as starting at noon and ending at noon the next day. A total of 224 fog episodes were identified on 153 foggy days, giving a total fog time of 561 h. Fog events were divided into three categories: short (up to 3 h, 158 episodes), medium (3–6 h, 46 episodes), and long (more than 6 h, 20 episodes). The mean duration of a single fog event was 150 min

(median 90 min, standard deviation 161 min). The longest event lasted 18 h, starting on 8 November 2020 at 23:00 UTC, and the shortest one was 30 min (19 January 2020).

Annual fog statistics are presented in Table 6. The number of fog events ranged from 5 in 2025 to 64 in 2020, with the most recent years (2023–2024) showing similar values of about 37–38 events per year (Figure 4b). The total annual fog time was highest in 2020 (178 h) and decreased to between 58 h and 95 h in 2022–2024 (Figure 4c). The mean per-event duration was relatively stable, ranging from 117 to 167 min in 2020–2024; 2025 stands out with only five events but the highest mean duration (276 min), driven by a few unusually persistent events. Although winter exhibits the fewest fog events, the longest-lasting episodes occur in February and November. This is likely related to the extended nighttime hours and low solar elevation angle during these months, which allow fogs to develop over a longer period and dissipate more slowly due to reduced solar heating.

Table 6. Annual fog statistics at $\text{SolarAOT}_{\text{lower}}$ (2020–2025).

Year	Fog Count	Foggy Days	Total [h]	Mean [min]	Median [min]	Longest [min]
2020	64	45	178.0	167	90	1080
2021	50	39	123.0	148	90	600
2022	30	17	58.5	117	60	510
2023	37	24	84.0	136	120	330
2024	38	25	94.5	149	60	780
2025	5	3	23.0	276	330	510

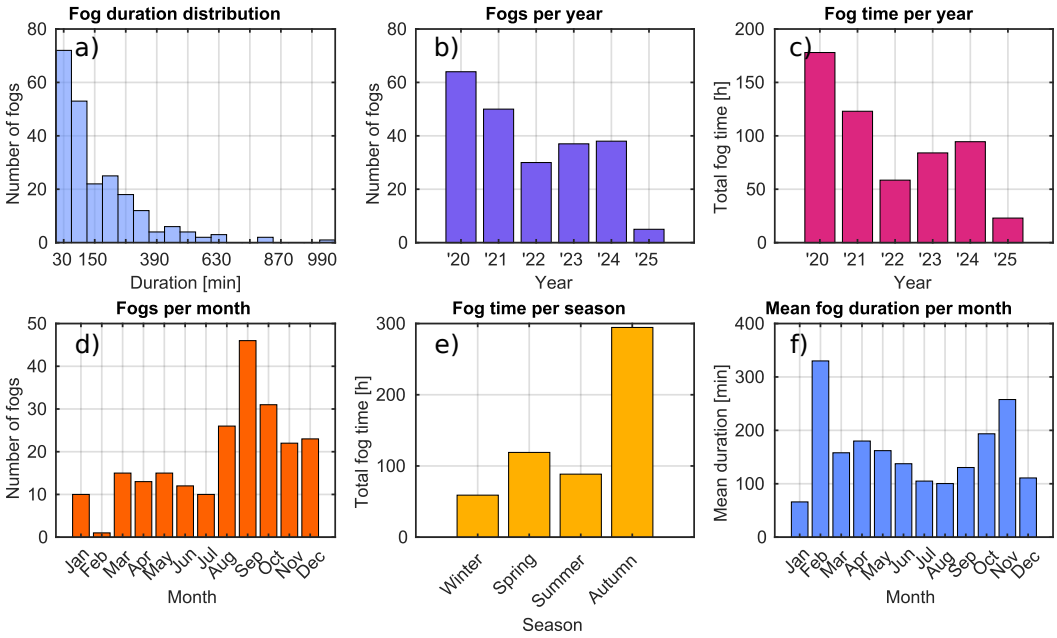


Figure 4. Fog statistics at $\text{SolarAOT}_{\text{lower}}$ (2020–2025). (**a**) Distribution of single-event fog duration (whole period). (**b**) Number of separate fog events per year. (**c**) Total fog hours per year. (**d**) Number of fog events per calendar month, summed across years. (**e**) Total fog hours per meteorological season (DJF/MAM/JJA/SON), summed across years. (**f**) Mean duration of a single fog event per calendar month (mean of individual event duration starting in that month, across all years; not cumulative time).

The seasonal distribution shows a clear autumn maximum (Figure 4d–f). Autumn (SON) had 99 events and 295 h of fog—more than the other three seasons combined—with the highest mean per-event duration (179 min). The other seasons have different rankings depending on whether we look at event count or total fog time: summer (JJA) had the second-largest event count (48), but the events were short (mean 111 min), giving a

cumulative 88.5 h. Spring (MAM) had fewer events (43) but they were substantially longer (mean 166 min), so the cumulative spring fog time (119 h) exceeded that of summer. Winter (DJF) had the fewest events (34), with December alone contributing 23 and February only one; combined with the shortest mean duration (104 min), winter accumulated only 59 h.

At monthly resolution (Figure 4d–f), the autumn peak splits into a primary maximum in September (46 events, 100 h total) followed by October (31 events, 100 h), December (23 events), November (22 events), and August (26 events). The longest mean per-event duration occurred in November (258 min), which is consistent with persistent radiative fogs typical for late autumn.

Diurnal Cycle of Fog

The vast majority of fog events occurred between 18:00 and 06:00 UTC (UTC = LT-2 for spring and summer, UTC = LT-1 in autumn and winter, where LT is local time). The diurnal distribution of observed fog shows a continuous increase from late evening until a peak around 03:15, followed by a steady decline after 04:15. A secondary, smaller peak appears between 15:45 and 16:45, likely corresponding to advective or valley fogs forming in the afternoon.

Fog events of different duration show distinct diurnal patterns (Figure 5b,c). Long fogs typically begin before 22:00 and dissipate around 05:45. Medium-duration fogs start slightly after midnight 00:15, and dissipate earlier, near 04:30. Short fogs show the broadest range of onset and dissipation times, although on average, they start around 01:20 and dissipate around 02:30.

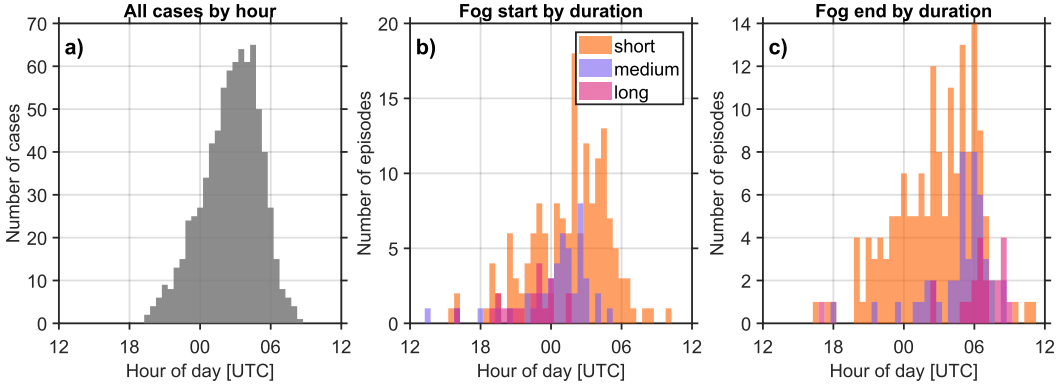


Figure 5. Timing of fog occurrence at SolarAOT$_{lower}$ (2020–2025). (**a**) Hourly distribution of fog occurrences throughout the day. (**b**) Hourly distribution of fog onset times, colour-coded by duration. (**c**) Hourly distribution of fog dissipation times, colour-coded by duration.

4.2. Statistics of Microphysical Parameters

Microphysical parameters (LWP, COD^f, R_{eff}) were retrieved with the OE scheme described in Section 2.3.2. During the six-year measurement period, 1122 individual 30 min fog occurrences were identified. For 53 of these cases, the data were unavailable. Retrievals were performed for the remaining 1069 cases, of which 987 have the cost function below the χ^2 threshold. After removing the 217 cases in which the upper station was itself inside the cloud (Section 2.7), 770 cases remain, which corresponds to 72% of the processed cases. All statistics reported below are based on these 770 cases.

The number of fog occurrences at night (solar elevation angle below 10°) was 916, and retrievals were obtained for 677 of them. The number of fog occurrences during the day (solar elevation angle above 10°, as used throughout this paper to define daytime cases) was 153, and retrievals were obtained for 93 cases. Cloud above the fog was identified in 360 cases (47% of the sample), where night cases were 307 and day 53. For daytime cases, R_{eff} and LWP are normally retrieved using both SW and LW channels. However,

when clouds are present above the fog, the optical thickness matching of those clouds accounts only for the LW agreement at cloud top. Therefore, for daytime cases with clouds, only LWP was retrieved (53 cases), while in the remaining 40 cases, both R_{eff} and LWP were retrieved.

4.2.1. Liquid Water Path (LWP)

Figure 6 presents the LWP statistics for all fog episodes, divided into short, medium, and long fogs. The mean LWP over the full six-year period is 21.4 $\pm$ 5.3 g m^{-2} for nighttime cases and 22.8 $\pm$ 5.1 g m^{-2} for daytime cases.

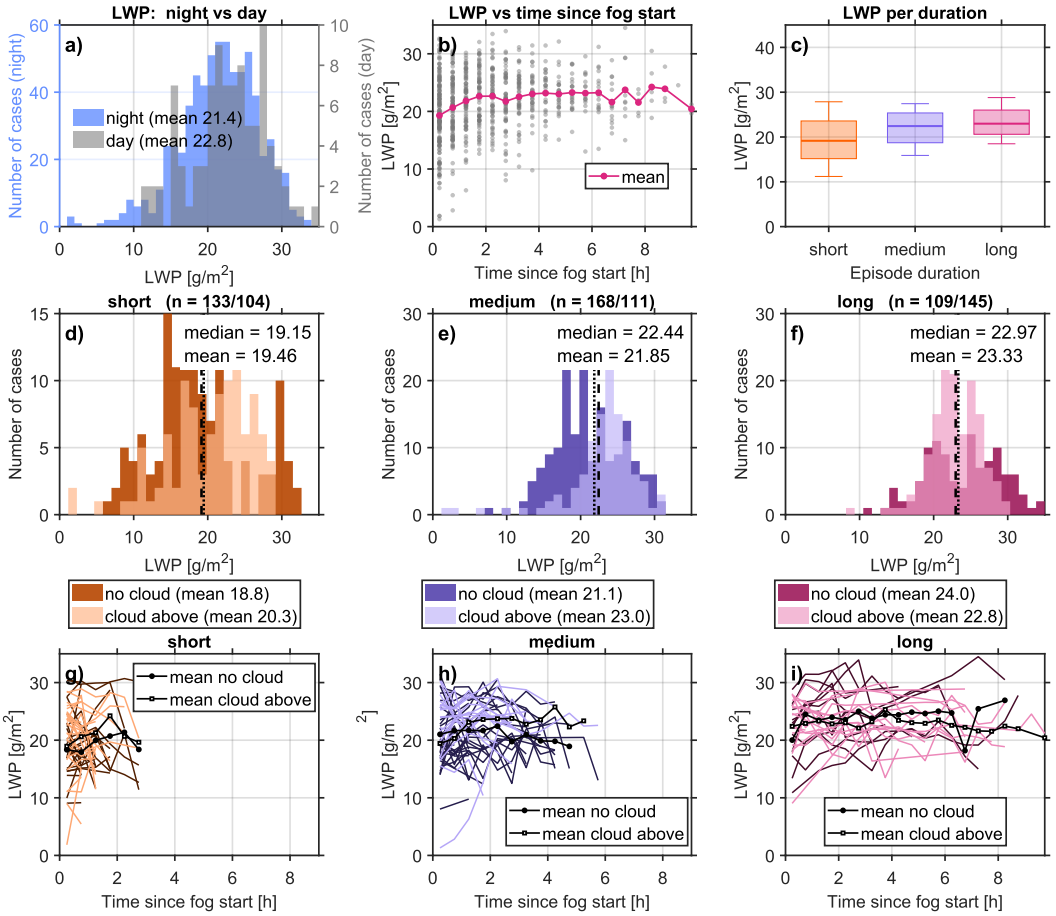


Figure 6. LWP statistics for all 770 good quality retrievals (n = without/with a cloud above the fog). (**a**) Histogram of all LWP values with the frequency of occurrence, separated into nighttime (blue) and daytime (grey) cases. (**b**) LWP evolution with time since fog onset. (**c**) Median LWP depending on the fog duration category. Panels (**d**–**f**) show LWP histograms for (**d**) short, (**e**) medium, and (**f**) long fogs. Panels (**d**–**i**) have two colour shades: darker denoting cases without cloud above and lighter shades representing cases with a cloud above. Panels (**g**–**i**) show the time evolution of the mean LWP depending on fog duration. The thick black line represents the mean (full dots—no cloud above; empty rectangle—cloud above fog), and the thin light lines represent individual cases.

The DFS for LWP averages 0.64 $\pm$ 0.24, lower than during the September 2023 campaign (0.73 at night). The difference is explained by overlying clouds: in 47% of the long-term cases, an additional cloud layer is detected above the fog, which raises the clear-sky reference at 185 m; if the overlying cloud is optically thick, it already emits nearly as a blackbody in the longwave window, so the fog beneath it adds little thermal contrast at the surface. The mean DFS$_{\mathrm{LWP}}$ is 0.79 (median 0.84) without an overlying cloud, compared to 0.47 (median 0.45) with one, and none of the 38 campaign cases had a cloud above the

fog. In both data sets, the DFS also decreases for the optically thickest fogs, for which the longwave signal saturates ($\epsilon \to 1$).

As can be seen from Figure 6, the mean LWP increases with fog duration: 19.5 $\pm$ 6.1 g m^{-2} for short fogs, 21.8 $\pm$ 4.8 g m^{-2} for medium fogs, and 23.3 $\pm$ 4.2 g m^{-2} for long fogs. These differences are statistically significant (Wilcoxon pairwise rank-sum, $p_{\text{Wilcoxon}} < 0.01$). Short-lived fogs exhibit a roughly symmetric distribution, medium fogs a left-skewed LWP distribution (median 22.4 g m^{-2}), while long-lived fogs are right-skewed (median 23.0 g m^{-2}).

Short fogs, no cloud above, start with a mean LWP of 18.3 g m^{-2}, which increases over time until 2 h 15 min after onset, when they reach a mean LWP of 21.4 g m^{-2}. During the final half an hour, the LWP decreases back to 18.4 g m^{-2}. Short fogs with a cloud above follow the same rise-and-fall pattern, but shifted to higher values: they start at 18.9 g m^{-2}, peak at 24.2 g m^{-2} after 1 h 45 min, and drop to 19.6 g m^{-2} in the final half an hour. The LWP for medium fogs (no cloud) rises from 21.0 g m^{-2} in the first 2:15 h to 22.4 g m^{-2} and then starts to decline to 19.0 g m^{-2}. The medium fogs LWP with a cloud above stay above the cloud-free ones over almost their whole lifetime: they start at 19.4 g m^{-2}, rise to 23.1 g m^{-2} within the first 1 h 15 min, then stay between 22.8 and 23.8 g m^{-2}, reach a maximum of 25.8 g m^{-2} at 4 h 15 min, and end at 23.4 g m^{-2}.

For long fogs, no cloud above, after an onset at LWP equal to 20.0 g m^{-2}, the LWP quickly rises and stays between 23.5 and 25.0 g m^{-2} for the first 6 h 15 min after onset. For fogs lasting longer than 6 h, LWP can reach 26.9 g m^{-2}. For long fogs with a cloud above, the LWP remains steady over the first 3 h 15 min, varying between 22.1 and 25.3 g m^{-2}. After that, it decreases slowly with time, reaching 20.4 g m^{-2} after 9 h 45 min. In the long-duration class, the fogs with an overlying cloud persist longer and keep a slightly lower mean LWP than the cloud-free ones (22.8 against 24.0 g m^{-2}, Mann–Whitney $p = 0.065$), because the upper cloud layer shields the fog from solar heating after sunrise and slows its dissipation. In the short- and medium-duration classes, the ordering is reversed: fogs with a cloud above have a higher mean LWP than the cloud-free ones (20.3 against 18.8 g m^{-2} for short fogs, $p = 0.007$, and 23.0 against 21.1 g m^{-2} for medium fogs, $p = 3 \times 10^{-5}$), so a cloud above the fog does not lower the fog LWP in general; it accompanies the longest, most persistent episodes.

The LWP values at the beginning and end of each fog episode do not drop to zero. This is caused by the data processing method, in which the data are averaged over a 30 min window. The formation and dissipation of fogs at this location occur on a timescale of tens of minutes, which prevents these processes from being resolved.

The temporal evolution of all fogs from onset, shown in Figure 6b, indicates that fogs typically begin with a mean LWP of 19.3 g m^{-2}. During the first 2 h 15 min, LWP increases at a rate of +1.7 g m^{-2} h^{-1}, then from 2 h 15 min till 6 h 15 min, the rate drops to +0.27. After 6 h 15 min, the mean decreases slowly, at -0.3 g m^{-2} h^{-1}, based on a small number of long-lived episodes.

An analogous figure to Figure 6 showing COD^f is provided in Appendix B (Figure A1). It is not discussed in detail here because the relationship between LWP and COD^f is nearly linear (see Figure 7), but it is included for readers interested in COD^f values. Mean COD^f is 3.1 $\pm$ 0.8 for nighttime and 3.3 $\pm$ 0.7 for daytime cases, with values ranging from 0.2 to 5.

The status of R_{eff} is different from that of LWP and is best described as an observability limit of the method. A joint retrieval of LWP and R_{eff} was attempted for the 40 cases in which it is possible at all (daytime, solar elevation above 10°, no clouds above the fog). In all of them, the retrieved R_{eff} stayed at the a priori value of 10.79 µm within its uncertainty (right panel of Figure 7), the DFS for R_{eff} remained close to zero, and the

posterior uncertainty (1.8 µm) is barely below the prior one (1.9 µm). The joint retrieval therefore did not yield R_{eff} retrievals that are independent of the prior; R_{eff} is shown in Section 4.2.2 for completeness only, and LWP is the parameter that this configuration actually constrains.

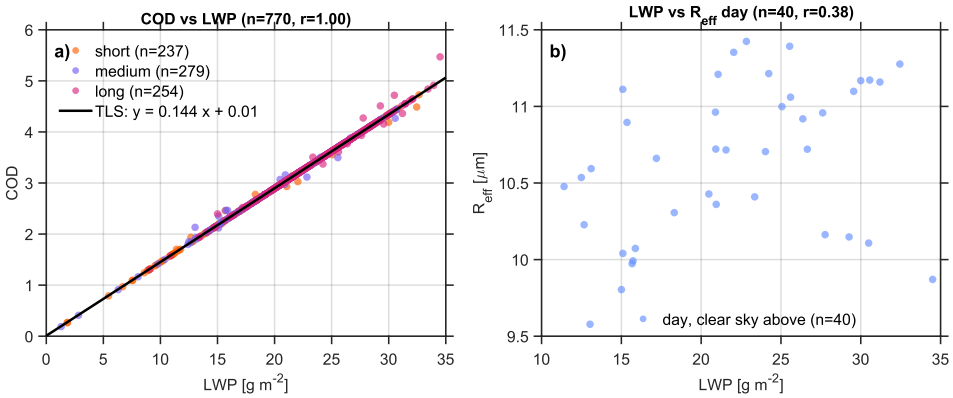


Figure 7. Panel (**a**) presents the dependence of COD^{f} on LWP, and the panel (**b**) the dependence of R_{eff} on LWP (retrieved only from daytime cases with no cloud present).

This limitation reflects the information content of broadband fluxes and the error budget of the inversion rather than the longwave channel as such. By day, the shortwave difference adds a second observable that responds to $\mathrm{COD} \propto \mathrm{LWP}/R_{\mathrm{eff}}$, but the sensitivity of $\Delta SW^{\downarrow}$ to R_{eff} at fixed LWP is small compared with the pyranometer uncertainties entering $\mathbf{R}$, so the prior term of the cost function dominates. A linear analysis with the stored Jacobians shows what would be needed to change this: a reduction of the shortwave error alone does not help, because the responses of the two fluxes to LWP and R_{eff} are nearly proportional (Section 3.1), and R_{eff} would become observationally informative only if the errors of both channels were reduced by about an order of magnitude, to about 1 $\mathrm{W\,m^{-2}}$, which is beyond broadband radiometry; higher solar elevations within the range observed here (10–30°) do not change this picture. Spectrally resolved longwave radiances measured by AERI-class interferometers avoid this degeneracy, because the spectral dependence of the emissivity across the atmospheric window carries an R_{eff} signal not contained in the broadband fluxes; such retrievals constrain fog particle effective radius once the visible optical depth exceeds about 0.25 [11]. Our mean COD^{f} of 3.1 ± 0.8 is well above that threshold, so the missing constraint lies in the class of instrument and in its error budget, not in the optical thickness of the fog.

In addition to the 2D simulations, we performed 1D simulations retrieving LWP alone, to check whether retrieving a second parameter biased the LWP results. The maximum difference between the two approaches was 3.8 $\mathrm{g\,m^{-2}}$, with a bias of -0.9 $\mathrm{g\,m^{-2}}$ (2D minus 1D) and an RMSE of 1.4 $\mathrm{g\,m^{-2}}$.

4.2.2. Annual and Seasonal Variability of Microphysical Parameters

Figure 8 presents the multi-annual and seasonal variability of the three retrieved fog properties—LWP, R_{eff} (day cases only; prior-dominated and shown for completeness, see Section 4.2.1) and COD^{f}. Each panel combines two visualisations: coloured box-and-whisker plots showing the distribution of the retrieved quantity, and grey bars showing the number of fog cases per bin.

The seasonal distribution (Figure 8d–f) shows a strong preference for autumn: SON contributes 418 cases, roughly twice as many as MAM (192) and nearly three times as many as JJA (148). Winter (DJF) provides only 12 cases after the exclusion described in Section 2.7, too few for a seasonal statement, and almost none of them satisfy the el $\geq 10°$

criterion required for the SW-based R_{eff} retrieval (Figure 8e essentially empty for DJF). This pattern is consistent with the well-established climatology of radiation fog in central Europe: long, cold, calm autumn nights combined with high near-surface moisture provide the most favourable conditions for radiative cooling to reach the dew point. Summer daytime heating limits fog formation, and winter is dominated by advection stratus or by frontal cloud that limits radiation cooling.

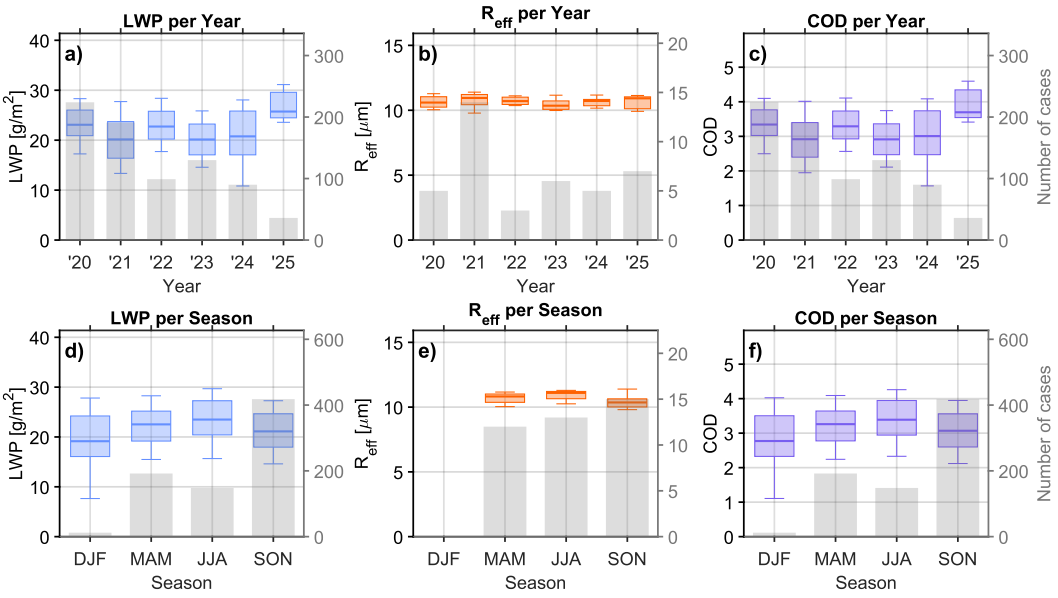


Figure 8. Multi-annual and seasonal variability of the retrieved fog properties ($n = 770$ for LWP and COD^f, 40 for R_{eff}). Panels (**a**–**c**) show box-and-whisker plots of LWP, R_{eff} (prior-dominated, shown for completeness), and COD^f by year. Panels (**d**–**f**) show the same quantities by meteorological season (DJF/MAM/JJA/SON). Grey bars indicate the number of fog cases per bin.

The number of fog cases per year (Figure 8a–c) is uneven. The years 2020 and 2021 dominate the sample, whereas 2022–2024 contribute markedly fewer events (∼90–130). The year 2025 sample comprises only 36 cases. This year-to-year contrast is dominated by inter-annual synoptic variability rather than by any instrumental gap: the retrieval configuration is identical across all years and the observation site (Strzyżów) operates continuously.

LWP shows small but statistically significant differences: medians are close to 22 g m^{-2} throughout, with 2025 slightly elevated (25.7 g m^{-2}, Figure 8a) and the seasonal medians ranging from 19.1 g m^{-2} (DJF, only 12 cases) to ∼23.5 g m^{-2} (JJA, Figure 8d). Part of this flatness is imposed by the common prior. When the prior covariance is relaxed by a factor of four, the seasonal medians spread from 19.4 to 26.9 g m^{-2}, and the inter-annual spread grows from 5.6 to 8.5 g m^{-2} (Table 4). The level itself is robust: the all-case median moves by less than 1 g m^{-2} under the same relaxation. This general consistency is confirmed when the dataset is restricted to observation-dominated cases and to the no-cloud subset (Appendix C).

Although the majority of fog events occur in autumn, the highest LWP values are recorded in summer. The higher frequency of fog in autumn is likely related to the seasonal shift in the radiative budget: decreasing incoming shortwave radiation combined with outgoing longwave radiation from the surface still warmed by summer leads to strong nocturnal cooling, bringing the air temperature closer to the dew point. In summer, the higher near-surface temperatures result in a larger saturation vapour pressure, so when fog forms, the fog layer contains more liquid water. This produces thicker fog episodes, leading to a broader spread in the summer data.

Because R_{eff} remains close to its a priori value and $\mathrm{COD}^f \propto \mathrm{LWP}/R_{\mathrm{eff}}$, the COD^f variability (Figure 8c,f) mirrors that of LWP. The differences between years and between seasons are statistically significant (Kruskal–Wallis test for LWP: $p = 10^{-18}$ between years and $p = 7 \times 10^{-6}$ between seasons), but this reflects the large sample size rather than a large effect: the medians of individual years or seasons differ by only a few g m^{-2}, which is well within the spread of LWP among the cases of any single year or season.

Summarising the long-term picture at Strzyżów: fog occurrence is strongly modulated by year and season, being most frequent in autumn and in the 2020–2021 period, whereas the microphysical characteristics of the fog droplets (both R_{eff} and the resulting LWP–COD^f range) are only weakly modulated. This decoupling between the frequency of fog events and their instantaneous optical properties is a useful constraint for regional climate applications: year-to-year and seasonal changes in the fog radiative forcing are primarily controlled by how often the fog forms rather than by how thick it is when it does form.

4.2.3. LWP Comparison Between the OE Retrieval and the Stephens Parameterisation

Figure 9 compares the LWP from the Gauss–Newton retrieval with the LWP derived from Equation (13) using the measured $LW^{\downarrow}_{\mathrm{up}}$, $LW^{\downarrow}_{\mathrm{down}}$ and the cloud-base temperature T_{cb} (assumed as the ground temperature at the lower station). The dataset is separated into two subsets depending on the presence of a higher cloud layer.

For the clear-sky subset (no cloud above, n = 406), the retrieved LWP and the Stephens-derived LWP correlate reasonably well (PCC = 0.79); a total-least-squares fit gives a slope of 0.77 and a small offset of -1.7 g m^{-2}. The fitted broadband absorption coefficient ($a_0^{\mathrm{fit}} = 0.108$ m^2 g^{-1}) is about 30% lower than the canonical value $a_0 = 0.158$ m^2 g^{-1}, which means the Stephens parameterisation tends to underestimate LWP—the mean bias is -6.6 g m^{-2}. Under an overlying cloud (n = 351) the fit is steeper (slope 1.08, offset -10.3 g m^{-2}, $a_0^{\mathrm{fit}} = 0.099$ m^2 g^{-1}). With the mean degrees of freedom for the cloud-above cases equal to 0.48, the retrieval still has enough dynamic range for the Stephens relation to be well defined even beneath a cloud. The scatter about the fitted line remains larger for the cloud-above subset (RMSE 8.9 vs. 7.5 g m^{-2}), even though the correlation itself is higher (PCC 0.86 vs. 0.79). This is because the upper-station longwave signal gets close to the cloud-base blackbody emission so the fog contrast becomes comparable to the $\approx$5 W m^{-2} measurement noise. The two-station optimal-estimation retrieval works better here since the overlying cloud is modelled explicitly through its optical depth.

The Stephens formula underestimates LWP because the original parameterisation assumes a mass extinction coefficient that is too high for the observed fog. This discrepancy is visible across the entire LWP range.

The $\sim$30% reduction of the fitted absorption coefficient can be explained by the droplet size distribution. The coefficient a_0 integrates the Mie absorption cross-section over the droplet size distribution, so its value depends on both the effective radius and the width of this distribution. The Stephens value of 0.158 m^2 g^{-1} is a single fit to eight cloud models spanning a wide range of microphysics. We reconstructed the drop-size distributions of these models (modified gamma functions, with parameters determined from the droplet concentration, liquid water content, and mode radius listed by Stephens [50]) and repeated the Mie calculation for each of them. An absorption-only calculation with a diffusivity factor of 1.66 reproduces the fitted value on average ($a_0 = 0.151$ m^2 g^{-1} over the seven unimodal models), but the individual values ranged from 0.115 to 0.180 m^2 g^{-1}. The narrow small-droplet stratus and stratocumulus models ($R_{\mathrm{eff}} = 5.1$–6.0 µm) give 0.16–0.18 m^2 g^{-1}, whereas the models with effective radii comparable to our fog prior (Sc II, Ns, Cu;

R_{eff} = 9.8–11.4 µm) give only 0.115–0.130 m^2 g^{-1}. The same calculation for the log-normal distribution fitted to our measurements (R_{eff} = 10.79 µm, σ_g = 1.88) yields a_0 = 0.112 m^2 g^{-1}.

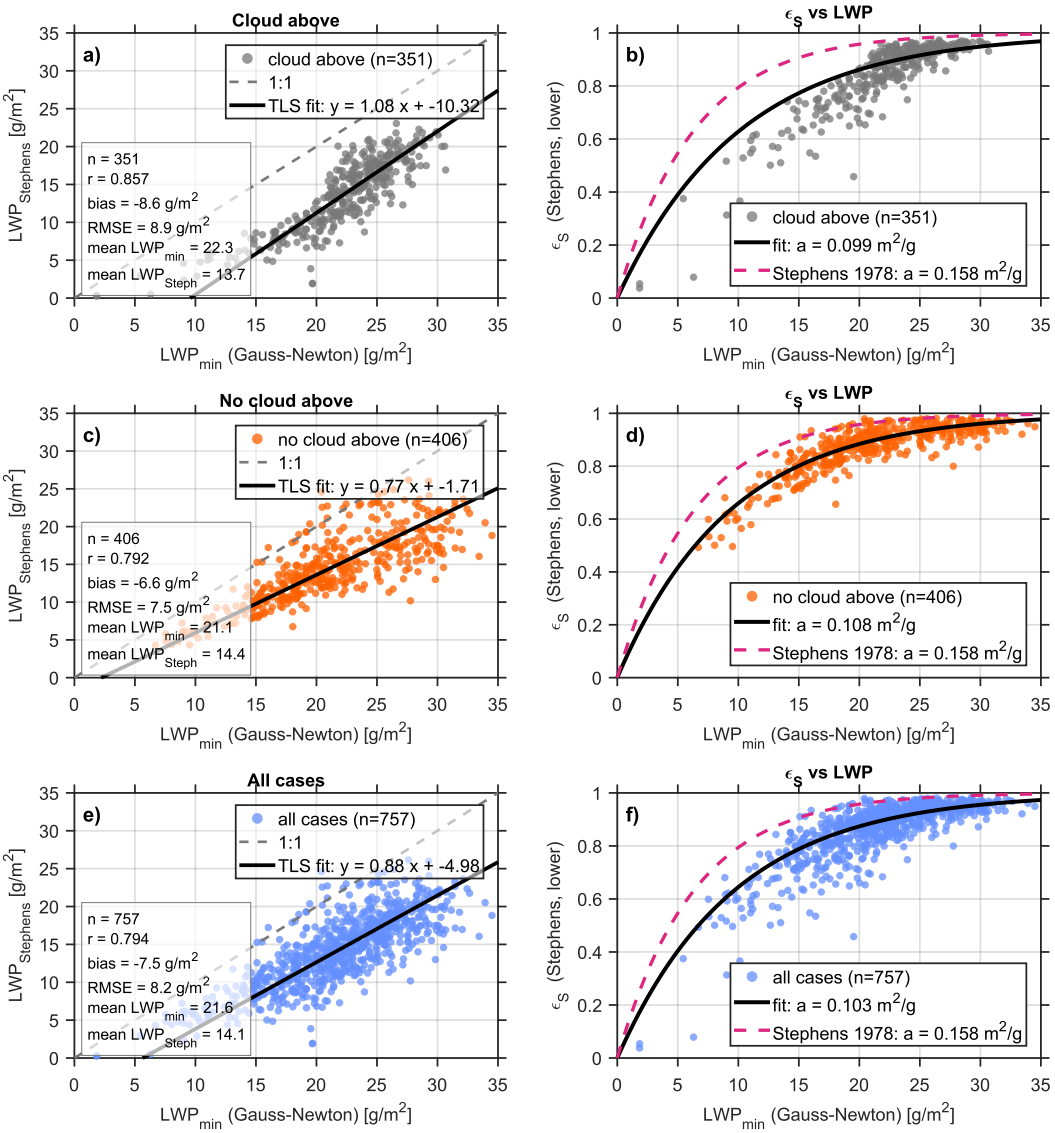


Figure 9. Comparison of the retrieved LWP with the LWP derived from the Stephens parameterisation. Panels (**a**,**b**) show cases with a cloud layer above the fog, while panels (**c**,**d**) show cases with clear sky above the fog; panels (**e**,**f**) show all cases together (with clear and cloudy conditions above the fog). The left column presents the dependence of LWP from the Stephens parameterisation on LWP from the OE retrieval, and the right column the dependence of emissivity calculated from Equation (11) on LWP from the OE retrieval.

Most of the departure from 0.15 m^2 g^{-1} is related to an effective-radius effect already present within the Stephens model set. The absorption cross-section efficiency Q_{abs} depends on the size parameter $x = \frac{2\pi R}{\lambda}$; for the thermal infrared wavelength range around 10 µm, corresponding to the peak of the Earth's thermal emission, fog droplets with radii of several micrometres have x values large enough that Q_{abs} approaches saturation values (close to one). For this reason, the absorption per unit mass—and hence a_0—scales approximately as $1/R_{\mathrm{eff}}$. The remaining part comes from the width of the distribution: all of the Stephens models are narrow, while our fitted distribution is considerably broader. For a fixed R_{eff} of 10.8 µm, broadening alone lowers a_0 by about 8% (from 0.122 to 0.112 m^2 g^{-1}). This happens because mass is shifted into large droplets whose absorption per unit mass decreases as

$1/R$. For this reason, a reduced effective a_0 for a mature fog with large droplets is consistent with the Stephens framework itself.

4.2.4. Relationship Between Fog Emissivity and LWP

Figure 10 shows the dependence of the retrieved fog LWP on the atmospheric emissivity derived from the fluxes at the upper station, $\epsilon_{\mathrm{top}} = LW^{\downarrow}_{\mathrm{up}}/(\sigma T^4_{\mathrm{up}})$. For the full dataset ($n = 770$), the dependence is weak: the correlation is PCC $= -0.11$ and the linear fit gives a slope of only $-9.2\ \mathrm{g\,m^{-2}}$ per unit of emissivity, with a median ϵ_{top} of 0.81. There is no threshold behaviour either: the median LWP is 22.1 $\mathrm{g\,m^{-2}}$ for $\epsilon_{\mathrm{top}} < 0.80$ ($n = 342$), 22.2 $\mathrm{g\,m^{-2}}$ for $0.80 \le \epsilon_{\mathrm{top}} < 0.90$ ($n = 284$) and 21.6 $\mathrm{g\,m^{-2}}$ for $0.90 \le \epsilon_{\mathrm{top}} < 0.95$ ($n = 142$), a spread that is only at the limit of significance (Kruskal–Wallis $p = 0.05$). A reduction of the fog-top cooling by an overlying cloud, which is the main driver of radiation fog formation [53,54] and which was reported for the SIRTA observatory by Wærsted et al. [55] and in the PARISFOG field campaign overview [56], is expected on physical grounds, but is not resolved by our data.

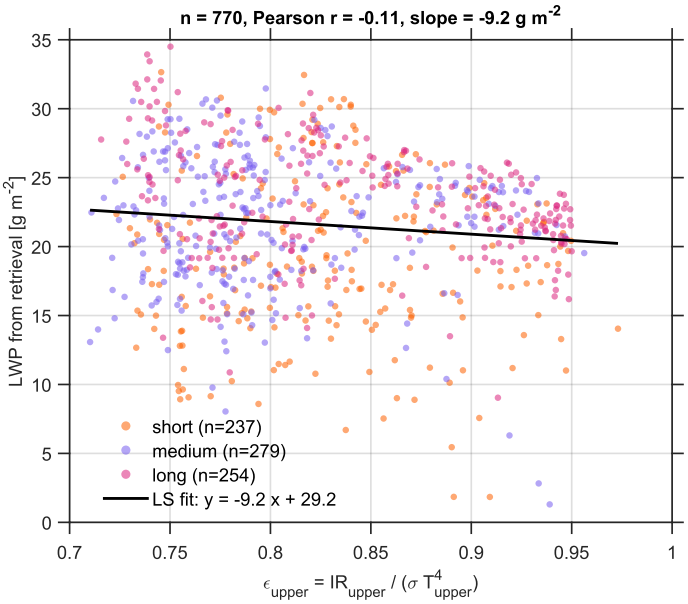


Figure 10. Dependence of the retrieved fog LWP on the emissivity at the SolarAOT$^{\mathrm{upper}}$ station (above fog). Black line indicates the least-squares fit to the data. Colours represent the fog duration. $n = 770$; cases with the upper station inside the cloud excluded.

For low emissivity values, the scatter is much larger. Without a cloud above the fog, the LWP depends on many things besides the radiative boundary condition at the top. Turbulent mixing driven by wind shear, the strength of the surface-based inversion and the availability of moisture in the boundary layer all modulate the fog thickness [2,57,58]. The cases are separated by duration (short, medium, and long, distinguished by colour). We do not see a dependence on duration either.

5. Discussion

The averaging kernel and the DFS reported for every case show where the method is observation-dominated and where it is prior-dominated, and three conditions control the outcome. The first is the COD^f itself: the averaging kernel for LWP is 0.8–0.9 below 20 $\mathrm{g\,m^{-2}}$ but falls to 0.4–0.5 above it, because the longwave emissivity of the layer saturates, so the retrieval of thick fogs (LWP above about 30 $\mathrm{g\,m^{-2}}$) is increasingly set by the prior. The second is an overlying cloud, which halves the information content (median DFS$_{\mathrm{LWP}}$ 0.45 against 0.84 without cloud), because the fitted COD absorbs part of the longwave

signal. The third is the position of the upper station, which must be above the fog: when it is inside the cloud, the retrieval collapses onto the prior (median DFS_{LWP} 0.19), which is why such cases were excluded. For LWP above about 30 g m^{-2}, the retrieval becomes less reliable, because the radiative signal saturates and the cost function is less sensitive to changes in liquid water.

The retrieval of R_{eff} is prior-dominated under all conditions: its averaging kernel is close to zero and the posterior uncertainty (1.8 µm) remains close to the prior one (1.9 µm), so the daytime R_{eff} values should be read as a consistency check rather than as a retrieved quantity. Broadband radiometers therefore constrain LWP but not the droplet size, because both fluxes respond mainly to the optical depth of the layer; resolving R_{eff} would require either flux errors of both channels about an order of magnitude smaller than those of the present radiometers, or spectrally resolved longwave radiances. For R_{eff}, a sensitivity test showed that different R_{eff} values produce different radiative signals for a fixed LWP. Out of six years of observations, only 40 cases allowed a joint retrieval of LWP and R_{eff} at all, and even in these, R_{eff} stayed at its prior value; the method therefore does not provide an independent retrieval of R_{eff}. A major reason for the small number of successful retrievals is the frequent presence of cloud layers above the fog.

The DFS_{LWP} for the full dataset is approximately 0.67 and increases to 0.79 for clear-sky-only cases. A dedicated prior-sensitivity analysis (Section 3.3.1) shows that this level of about 22 g m^{-2} is set by the observations—a fourfold weaker prior moves the median by about 1 g m^{-2}—whereas the apparent flatness of the seasonal and inter-annual cycle is partly imposed by the common prior, which compresses the seasonal spread from 7.4 to 4.3 g m^{-2}. The qualitative conclusion is unaffected, because even the uncompressed spread of 19–27 g m^{-2} is small compared with the year-to-year variability of fog occurrence.

Cloud layers above the fog are common in the study area and they complicate the retrieval. To address this problem, the retrieval scheme includes an additional COD parameter, retrieved by minimising the difference between modelled and observed LW fluxes at the upper station. With this correction, we can process many nighttime events, but the daytime retrieval of two parameters is restricted to clear-sky cases only. The reason is that the cloud above the fog is constrained by LW measurements, so its SW properties remain undetermined. Without the overlying cloud correction, a large fraction of fog events would be excluded entirely; however, the simplified treatment of midlevel clouds limits the applicability of the two parameters daytime retrieval, as more than half of the daytime cases exhibit overhead cloud cover.

The two stations are 4.06 km apart, but the retrieval requires horizontal uniformity only of the atmosphere above the fog top, not of the fog itself; with a median wind of 2.5 m s^{-1} above the fog the air needs about 27 min to cross this distance, comparable to the 30 min case window, and neither the misfit nor the information content of the retrieval degrades with increasing wind speed.

In 22% of the fog cases, mostly in autumn and winter, the upper station was itself inside the cloud layer, as identified from its humidity and sky emissivity and confirmed by the station camera. These retrievals were prior-dominated (median DFS_{LWP} 0.19) and were excluded; their removal raises the six-year median LWP from 20.9 to 22.0 g m^{-2} and the median DFS_{LWP} from 0.58 to 0.67.

For the clear-sky cases (no overlying cloud), the Stephens formula Stephens [51] LWP versus the retrieved LWP yields a slope of 0.77 and an offset of -1.7 g m^{-2}. This corresponds to an effective mass extinction coefficient $a_0 = 0.108$ m^2 g^{-1}, lower than the canonical value 0.158 m^2 g^{-1}. In the presence of overlying clouds, the Stephens formula is similar, however the points are more scattered.

The two-station retrieval can be compared with the three ground-based techniques commonly used for fog liquid water. Microwave radiometers are the LWP reference, with an RMSE of 5–10 g m^{-2} in thin fog [6,55] and systematic model differences of 15–30 g m^{-2} [15]; the present posterior uncertainty (median 6.3 g m^{-2}) and the empirical RMSE of 5.4 g m^{-2} against tethered-balloon profiles are of the same order, though this profiles come from a single three-day campaign. The two methods fail at opposite ends of the LWP range: microwave retrievals exclude LWP below 10 g m^{-2} [6], whereas the broadband longwave signal used here saturates above ∼30 g m^{-2}. Adding a cloud radar gives the vertical LWC profile (uncertainty 0.05–0.06 g m^{-3} in SOFOG3D [59]), but radars cannot see below ∼40 m above ground [5], leaving the lowest part of the fog layer—which the dual-height configuration targets—uncovered. Only spectrally resolved infrared radiometers also constrain droplet size, with R_{eff} uncertainties below 20% [11,18]; the broadband fluxes used here contain no such spectral information, so R_{eff} remains at its prior under all conditions (Section 3.3.2). The advantage of the present configuration is that two pairs of broadband radiometers are inexpensive, operate unattended for years, and deliver LWP and COD^{f} every 30 min with a per-case measure of information content—a low-cost complement to microwave radiometers and cloud radars for long-term fog monitoring where such instruments are unavailable.

6. Conclusions

In this article, we presented a two-station, broadband-radiometric method for retrieving the liquid water path (LWP) and optical depth (COD^{f}) of radiation fog, and tested its ability to resolve the effective radius (R_{eff}), using the vertically separated stations (185 m altitude difference and an approximately 4 km horizontal offset) in the Strzyżów Valley and an optimal-estimation retrieval with the Fu–Liou radiative transfer model.

The retrieval was validated independently against balloon-borne OPC-N3 profiles (9–11 September 2023), yielding a PCC of 0.71, an RMSE of 5.4 g m^{-2}, and a regression slope of 0.94 for LWP. Together with the per-case information content (DFS), this establishes LWP as the robust output of the method: over 2020–2025, the mean LWP remained stable 21.6 ± 5.3 g m^{-2}, the mean COD near 3.1 ± 0.8, and prior-dominated cases can be flagged and excluded via the DFS. The main reliability limit is the saturation of the broadband longwave signal above ∼30 g m^{-2}, where LWP becomes increasingly prior-dominated. R_{eff}, in contrast, could not be resolved; the retrieval returns the prior value under all conditions. It must therefore be supplied from the prior or from colocated in situ instruments.

The practical scope of the method is that of a low-cost, unattended fog monitor at fixed sites, operating around the clock—including at night—and particularly suited to valley topographies where shallow fog fills the basin below the upper station. It delivers LWP and COD^{f} every 30 min at the cost of two pairs of radiometers, and complements rather than replaces microwave radiometers and cloud radars at sites where such instruments are unavailable.

One idea for future work is to put radiometers and in situ sensors (like OPC-N3, RS41, visibility sensors) on drones. Measuring fluxes at different heights inside the fog would allow the radiative closure for SW and LW to be checked by comparing the observed flux differences with model predictions based on the in situ microphysical parameters. This would add to what ground-based retrievals can tell us, and give validation at heights we cannot reach from the surface. The sensors are getting lighter, so this is becoming more realistic.

Author Contributions: Conceptualization, K.N. and K.M.M.; methodology, K.N.; software, K.N.; validation, K.N.; formal analysis, K.N.; investigation, K.N.; data curation, K.N.; writing—original draft preparation, K.N.; writing—review and editing, K.N. and K.M.M.; visualization, K.N.; supervision, K.M.M. All authors have read and agreed to the published version of the manuscript.

Funding: This research is part of the OPUS project (Polish Grant No. 2017/27/B/ST10/00549) Impact of aerosol on the microphysical, optical and radiation properties of fog, which was funded by the National Science Centre, coordinated by the Institute of Geophysics, Faculty of Physics, University of Warsaw.

Data Availability Statement: The raw data supporting the conclusions of this article will be made available by the authors on request.

Acknowledgments: We thank the AERONET team, principal investigators, and other participants for their effort in establishing and maintaining the network. This study contains modified Copernicus Climate Change Service information [39]. Neither the European Commission nor ECMWF is responsible for any use that may be made of the Copernicus information or data it contains.

Conflicts of Interest: The authors declare no conflicts of interest. The funders had no role in the design of the study; in the collection, analyses, or interpretation of data; in the writing of the manuscript; or in the decision to publish the results.

Abbreviations

The following abbreviations are used in this manuscript:

$\mathbf{A}$	Averaging kernel matrix
a_0	Mass absorption coefficient
AERI	Atmospheric Emitted Radiance Interferometer
AERONET	Aerosol Robotic Network
AOD	Aerosol optical depth
ARM	Atmospheric Radiation Measurement (programme)
a.s.l.	Above sea level
$\mathbf{B}$	Background error covariance matrix
BTD	Brightness temperature difference
CERES	Clouds and the Earth's Radiant Energy System
COD	Cloud optical depth
COD^f	Cloud optical depth of fog
DFS	Degrees of freedom for signal
DJF	Winter (December, January, February)
ECMWF	European Centre for Medium-Range Weather Forecasts
el	Solar elevation angle
ϵ_S	Cloud emissivity
$\boldsymbol{\epsilon}$	Measurement error vector
ERA5	ECMWF Reanalysis, fifth generation
g	Asymmetry parameter
$\mathbf{G}$	Gain matrix
$\boldsymbol{\Gamma}_n$, $\tilde{\boldsymbol{\Gamma}}_n$	Gauss–Newton Hessian, undamped and damped
γ	Levenberg–Marquardt damping parameter
$H(\mathbf{x})$	Forward model operator
$\mathbf{I}$	Identity matrix
$J(\mathbf{x})$	Cost function
JJA	Summer (June, July, August)
$\mathbf{K}$	Jacobian matrix of the forward model
LT	Local time
LW	Longwave radiation
LWC	Liquid water content

LWP	Liquid water path
MAM	Spring (March, April, May)
ML	Machine learning
MODIS	Moderate Resolution Imaging Spectroradiometer
MWR	Microwave radiometer
N_c	Droplet number concentration
$n(r)$	Droplet size distribution
n	Number of cases
NWP	Numerical weather prediction
OE	Optimal estimation
PARISFOG	ParisFog field campaign at the SIRTA observatory
PBL	Planetary boundary layer
PCC	Pearson correlation coefficient
PM1.0, PM2.5, PM10	Mass concentration of particulate matter below 1.0, 2.5 and 10 µm
p_{Wilcoxon}	p-value of the Wilcoxon pairwise rank-sum test
Q_{abs}	Absorption efficiency factor
$\mathbf{R}$	Observation error covariance matrix
R_{eff}	Effective radius
RH	Relative humidity
RMSE	Root mean square error
RT	Radiative transfer
$\hat{\mathbf{S}}$	A posteriori error covariance matrix
Sc, Ns, Cu	Stratocumulus, nimbostratus, cumulus (Stephens cloud models)
SEVIRI	Spinning Enhanced Visible and Infrared Imager
ShadowGraph	Instrument Oxford Lasers VisiSize D30
σ	Standard deviation; Stefan–Boltzmann constant
SIRTA	Site Instrumental de Recherche par Télédétection Atmosphérique
$\text{SolarAOT}^{\text{upper}}$	Observation station located at 445 m a.s.l.
$\text{SolarAOT}_{\text{lower}}$	Observation station located at 260 m a.s.l.
SON	Autumn (September, October, November)
SSA	Single scattering albedo
SW	Shortwave radiation
SYRSOC	Synergistic Remote Sensing of Clouds (retrieval algorithm)
TOA	Top of the atmosphere
UAV	Unmanned aerial vehicle
UTC	Coordinated Universal Time
WMO	World Meteorological Organization
$\mathbf{x}$	State vector (true state)
$\hat{\mathbf{x}}$	Retrieved (a posteriori) state vector
$\mathbf{x}_b$	A priori (background) state vector
$\mathbf{y}$	Observation vector

Appendix A. Gauss–Newton Iteration with Levenberg–Marquardt Damping

The minimum of J is found iteratively using the Gauss–Newton method with Levenberg–Marquardt damping to ensure robust convergence. At iteration n, the forward model is linearised around the current state $\mathbf{x}_n$:

$$H(\mathbf{x}) \approx H(\mathbf{x}_n) + \mathbf{K}_n(\mathbf{x} - \mathbf{x}_n) \tag{A1}$$

where $\mathbf{K}_n = \partial H/\partial \mathbf{x}\big|_{\mathbf{x}_n}$ is the Jacobian matrix of the forward model evaluated at $\mathbf{x}_n$.

Substituting the linearisation into Equation (3) and setting $\nabla_{\mathbf{x}} J = 0$ yields the Gauss–Newton approximation to the Hessian:

$$\boldsymbol{\Gamma}_n = \mathbf{B}^{-1} + \mathbf{K}_n^{\mathrm{T}} \mathbf{R}^{-1} \mathbf{K}_n \tag{A2}$$

This approximation uses only first-order derivatives (the Jacobian $\mathbf{K}$), avoiding the computation of second derivatives of the forward model. It is exact when H is linear and provides a good approximation for weakly non-linear problems.

A Levenberg–Marquardt damping term is added to control the step size:

$$\tilde{\boldsymbol{\Gamma}}_n = \boldsymbol{\Gamma}_n + \gamma \, \mathrm{diag}(\boldsymbol{\Gamma}_n) \tag{A3}$$

where γ is the damping parameter. The state update is then

$$\mathbf{x}_{n+1} = \mathbf{x}_n + \delta \mathbf{x}_n \tag{A4}$$

where the increment $\delta \mathbf{x}_n$ is obtained by solving

$$\tilde{\boldsymbol{\Gamma}}_n \, \delta \mathbf{x}_n = \mathbf{K}_n^{\mathrm{T}} \mathbf{R}^{-1} (\mathbf{y} - H(\mathbf{x}_n)) - \mathbf{B}^{-1} (\mathbf{x}_n - \mathbf{x}_b) \tag{A5}$$

For large γ, $\tilde{\boldsymbol{\Gamma}}_n$ is diagonally dominated and the step reduces to a small gradient-descent update; as $\gamma \to 0$, the standard Gauss–Newton step is recovered. The candidate state $\mathbf{x}_{n+1}$ is accepted only if it reduces the cost function, i.e., $J(\mathbf{x}_{n+1}) < J(\mathbf{x}_n)$. Upon acceptance, γ is halved; if the step is rejected, γ is increased by a factor of 5 and the iteration is repeated from the same point. The damping parameter is initialised at $\gamma = 10$; if it exceeds 10^6 without a successful step, the minimisation is terminated.

The iteration stops when either (i) the relative change in the state vector falls below a convergence threshold:

$$\frac{\|\delta \mathbf{x}_n\|}{\|\mathbf{x}_n\|} < \delta_{\mathrm{tol}} \tag{A6}$$

with $\delta_{\mathrm{tol}} = 10^{-3}$, or (ii) the number of accepted steps reaches 20. The retrieved state is additionally bounded to physically meaningful ranges: $R_{\mathrm{eff}} \in [2, 20]$ µm and $\mathrm{LWC} \in [0, 0.5]$ g m^{-3} (equivalently, $\mathrm{LWP} \in [0, 0.5 \cdot \Delta z]$ g m^{-2}, where Δz is the fog layer thickness in metres).

Upon convergence, the *a posteriori* error covariance matrix is

$$\hat{\mathbf{S}} = \boldsymbol{\Gamma}_n^{-1} = \left(\mathbf{B}^{-1} + \mathbf{K}^{\mathrm{T}} \mathbf{R}^{-1} \mathbf{K} \right)^{-1} \tag{A7}$$

The posterior covariance uses the undamped Hessian $\boldsymbol{\Gamma}_n$, not the damped $\tilde{\boldsymbol{\Gamma}}_n$, because the damping is only a numerical trick and should not affect the uncertainty. The diagonal elements provide the retrieval uncertainties: $\hat{\sigma}_{\mathrm{LWP}} = \sqrt{\hat{\mathbf{S}}_{11}}$ and $\hat{\sigma}_{R_{\mathrm{eff}}} = \sqrt{\hat{\mathbf{S}}_{22}}$.

The posterior covariance can be split into the two contributions that appear in the uncertainty budget of Section 3.3.2. With the gain matrix $\mathbf{G} = \hat{\mathbf{S}} \, \mathbf{K}^{\mathrm{T}} \mathbf{R}^{-1}$ and the averaging kernel $\mathbf{A} = \mathbf{G}\mathbf{K}$, the error of the retrieved state $\hat{\mathbf{x}}$ with respect to the true state $\mathbf{x}$ is [34]

$$\hat{\mathbf{x}} - \mathbf{x} = (\mathbf{A} - \mathbf{I})(\mathbf{x} - \mathbf{x}_b) + \mathbf{G} \, \boldsymbol{\epsilon}, \tag{A8}$$

where the first term is the smoothing error, i.e., the part of the true departure from the prior that the observations cannot resolve and that is therefore filled in by the prior, and the second term is the measurement error $\boldsymbol{\epsilon}$ propagated through the retrieval. Their covariances are $(\mathbf{I} - \mathbf{A})\mathbf{B}(\mathbf{I} - \mathbf{A})^{\mathrm{T}}$ and $\mathbf{G}\mathbf{R}\mathbf{G}^{\mathrm{T}}$, and their sum is identical to $\hat{\mathbf{S}}$ of Equation (A7). Table 5

lists the square roots of the diagonal elements of the two terms separately; the degrees of freedom for signal used throughout the paper are the trace of **A**.

Appendix B. COD^f

Figure A1 presents the histograms of COD^f for short, medium and long fogs as well as change of COD^f in time from fog onset.

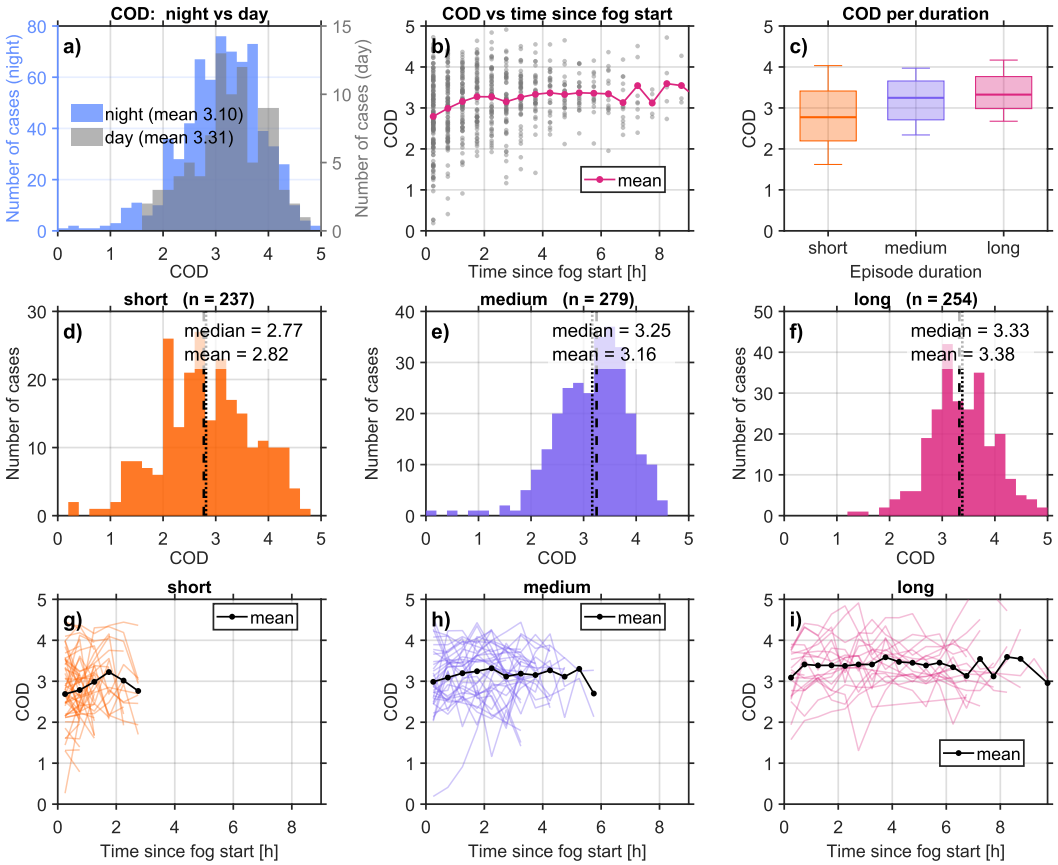


Figure A1. COD^f statistics for all good quality retrievals. (**a**) Histogram of all COD^f values with the frequency of occurrence, separated into nighttime (blue) and daytime (grey) cases. (**b**) COD^f evolution with time since fog onset. (**c**) Median COD^f depending on the fog duration category. Panels (**d**–**f**) show COD^f histograms for (**d**) short, (**e**) medium, and (**f**) long fogs. Panels (**g**–**i**) show the time evolution of the mean COD^f depending on fog duration. The thick black line represents the mean, and the thin light lines represent individual cases.

Appendix C. Influence of Clouds Above the Fog Layer

Figure A2 shows the retrieved LWP (left) and DFS (right) for cases with and without a cloud layer above the fog. Table A1 stratifies the retrieved LWP and COD^f by class of DFS$_{LWP}$. LWP for no-cloud-above cases is 21.1 $\pm$ 5.7 and with cloud above 22.1 $\pm$ 4.7 g m^{-2}. The mean LWP of the two populations differs by 1.0 g m^{-2}, which is statistically significant but small compared with the spread of either population (Mann–Whitney $p = 0.0002$, Cohen's $d = -0.19$; night-only control: $p = 0.0008$, $d = -0.17$), whereas their information content is very different (DFS$_{LWP}$ median 0.45 vs. 0.84, $d = 1.76$). Table A2 shows that the seasonal and annual statistics are essentially unchanged when only the no-cloud subset is used.

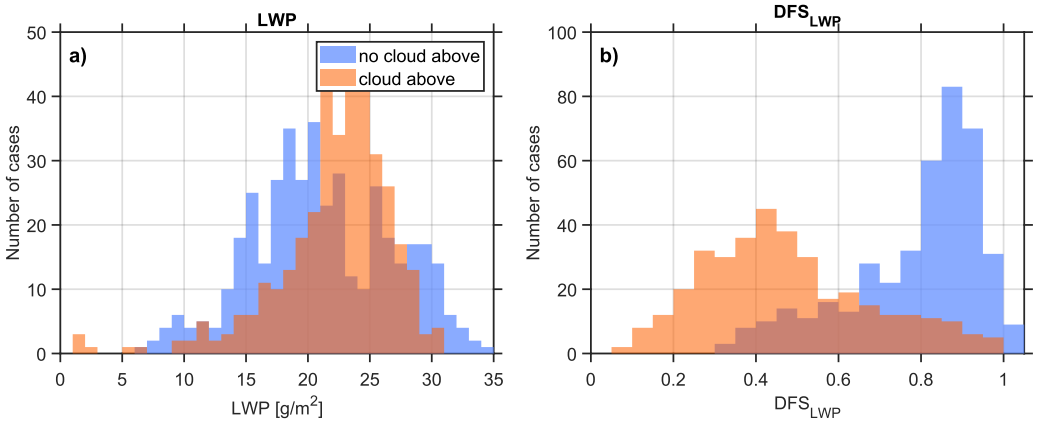


Figure A2. Histogram of LWP (**a**) and DFS (**b**) for cases with cloud above fog ($n = 360$, orange) and cases without clouds above fog ($n = 410$, blue). The mean LWP of the two populations (22.1 ± 4.7 and 21.1 ± 5.7 g m^{-2}) differs by only 1.0 g m^{-2}, while their information content differs strongly (median DFS 0.45 vs. 0.84).

Table A1. Retrieved fog properties stratified by the degrees of freedom for signal for LWP (DFS$_{LWP}$), for which the upper station was above the fog layer. $\langle|\text{LWP} - x_b|\rangle$ is the mean absolute departure of the retrieved LWP from the prior $x_b = 19.2$ g m^{-2}; values are mean $\pm$ standard deviation.

Class	n	LWP [g m^{-2}]	COD^f	$\langle\lvert\text{LWP} - x_b\rvert\rangle$ [g m^{-2}]
all good	770	21.6 ± 5.3	3.1 ± 0.8	4.7
DFS < 0.3	74	22.3 ± 2.2	3.2 ± 0.3	3.4
$0.3 \leq$ DFS < 0.5	184	25.4 ± 3.9	3.7 ± 0.6	6.4
DFS ≥ 0.5	512	20.1 ± 5.3	2.9 ± 0.8	4.3
DFS ≥ 0.7	363	18.2 ± 4.6	2.6 ± 0.7	3.6

Table A2. Seasonal and annual mean LWP [g m^{-2}] (mean $\pm$ standard deviation) for all cases and for the subset without a cloud layer above the fog. The agreement between the two columns shows that the long-term statistics are not affected by the lower information content of the cloud-above cases; the 2025 statistics are based on five episodes only.

	All Cases		No Cloud Above	
	LWP	n	LWP	n
DJF	18.9 ± 7.7	12	–	0
MAM	22.1 ± 5.1	192	21.6 ± 6.1	85
JJA	23.1 ± 5.3	148	23.7 ± 6.0	93
SON	20.9 ± 5.1	418	19.9 ± 5.0	232
2020	23.0 ± 4.6	224	22.6 ± 5.9	73
2021	20.0 ± 5.7	191	20.9 ± 4.9	123
2022	22.6 ± 4.4	99	22.5 ± 5.4	45
2023	20.0 ± 4.4	130	19.1 ± 4.7	92
2024	20.6 ± 6.1	90	19.4 ± 6.7	56
2025	26.9 ± 3.3	36	27.6 ± 3.7	21

Appendix D. Linear Evaluation of the Sensitivity to the Prior

The sensitivity to the prior (Section 3.3.1) was not obtained by re-running the retrieval, but from the converged solutions themselves. At convergence, the Gauss–Newton scheme of Appendix A satisfies

$$\hat{\mathbf{x}} = \mathbf{x}_b + \mathbf{G}\left[\mathbf{y} - H(\hat{\mathbf{x}}) + \mathbf{K}(\hat{\mathbf{x}} - \mathbf{x}_b)\right], \qquad \mathbf{G} = (\mathbf{K}^{\mathrm{T}}\mathbf{R}^{-1}\mathbf{K} + \mathbf{B}^{-1})^{-1}\mathbf{K}^{\mathrm{T}}\mathbf{R}^{-1}, \tag{A9}$$

where the Jacobian $\mathbf{K}$, the residual $\mathbf{y} - H(\hat{\mathbf{x}})$, $\mathbf{R}$ and $\mathbf{B}$ are stored for every case. Within the range over which $\mathbf{K}$ can be treated as constant, a different prior mean or prior covariance simply moves this minimum, and the new solution follows from Equation (A9) with $\mathbf{x}_b'$ or $\mathbf{B}'$ substituted, without any call to the radiative transfer model. For a shift of the prior mean, this reduces to $\mathbf{x}' = \hat{\mathbf{x}} + (\mathbf{I} - \mathbf{A})(\mathbf{x}_b' - \mathbf{x}_b)$ with $\mathbf{A} = \mathbf{GK}$; for a change of the prior covariance to $\mathbf{x}' = \mathbf{x}_b + \mathbf{G}'\mathbf{d}$ with $\mathbf{d} = \mathbf{y} - H(\hat{\mathbf{x}}) + \mathbf{K}(\hat{\mathbf{x}} - \mathbf{x}_b)$ and $\mathbf{G}'$ computed with $\mathbf{B}'$. In the one-dimensional nighttime case, $\sigma_{\text{post}} = \sigma_b\sqrt{1 - A}$ while the induced shift is $(1 - A)\,|\Delta\mathbf{x}_b|$, so a shift of the prior mean smaller than σ_b can never exceed the posterior uncertainty.

Two checks support the approximation. First, Equation (A9) reproduces the stored retrievals of the 770 retained cases to a median of 0.001 and a 99th percentile of 0.20 g m^{-2}, i.e., the iterations did converge to the minimum it describes. Second, in the synthetic experiment of Section 3.1, the full non-linear retrieval was run with the true LWP placed 5–11 g m^{-2} away from the prior; the resulting prior-induced offsets of -2.2 and $+0.24$ g m^{-2} (LWP = 24 and 8 g m^{-2}) compare with -2.1 and $+0.29$ g m^{-2} from the linear expression. The perturbations of Section 3.3.1 (± 4.8 and ± 9.6 g m^{-2}) lie within this validated range. The approximation is least accurate for the widest prior ($\mathbf{B}' = 10\mathbf{B}$), where the solution moves furthest from the point of linearisation; the conclusions of Section 3.3.1 are therefore based on $\mathbf{B}' = 4\mathbf{B}$. What the linear treatment cannot capture is a change in the set of cases passing the χ^2 acceptance test under a different prior.

References

1. Steeneveld, G.J.; Ronda, R.J.; Holtslag, A.A.M. The Challenge of Forecasting the Onset and Development of Radiation Fog Using Mesoscale Atmospheric Models. *Bound.-Layer Meteorol.* **2015**, *154*, 265–289. [CrossRef]
2. Gultepe, I.; Tardif, R.; Michaelides, S.C.; Cermak, J.; Bott, A.; Bendix, J.; Müller, M.D.; Pagowski, M.; Hansen, B.; Ellrod, G.; et al. Fog Research: A Review of Past Achievements and Future Perspectives. *Pure Appl. Geophys.* **2007**, *164*, 1121–1159. [CrossRef]
3. Long, Q.; Wu, B.; Mi, X.; Liu, S.; Fei, X.; Ju, T. Review on Parameterization Schemes of Visibility in Fog and Brief Discussion of Applications Performance. *Atmosphere* **2021**, *12*, 1666. [CrossRef]
4. Boutle, I.; Angevine, W.; Bao, J.W.; Bergot, T.; Bhattacharya, R.; Bott, A.; Ducongé, L.; Forbes, R.; Goecke, T.; Grell, E.; et al. Demistify: A large-eddy simulation (LES) and single-column model (SCM) intercomparison of radiation fog. *Atmos. Chem. Phys.* **2022**, *22*, 319–333. [CrossRef]
5. Delanoë, J.; Protat, A.; Vinson, J.P.; Brett, W.; Caudoux, C.; Bertrand, F.; du Chatelet, J.P.; Hallali, R.; Barthes, L.; Haeffelin, M.; et al. BASTA: A 95-GHz FMCW Doppler Radar for Cloud and Fog Studies. *J. Atmos. Ocean. Technol.* **2016**, *33*, 1023–1038. [CrossRef]
6. Vishwakarma, P.; Delanoë, J.; Jorquera, S.; Martinet, P.; Burnet, F.; Bell, A.; Dupont, J.C. Climatology of estimated liquid water content and scaling factor for warm clouds using radar–microwave radiometer synergy. *Atmos. Meas. Tech.* **2023**, *16*, 1211–1237. [CrossRef]
7. Costabloz, T.; Burnet, F.; Lac, C.; Martinet, P.; Delanoë, J.; Jorquera, S.; Fathalli, M. Vertical profiles of liquid water content in fog layers during the SOFOG3D experiment. *Atmos. Chem. Phys.* **2025**, *25*, 6539–6573. [CrossRef]
8. Dupont, J.C.; Haeffelin, M.; Wærsted, E.; Delanoë, J.; Renard, J.B.; Preissler, J.; O'Dowd, C. Evaluation of Fog and Low Stratus Cloud Microphysical Properties Derived from In Situ Sensor, Cloud Radar and SYRSOC Algorithm. *Atmosphere* **2018**, *9*, 169. [CrossRef]
9. Toledo, F.; Haeffelin, M.; Wærsted, E.; Dupont, J.C. A new conceptual model for adiabatic fog. *Atmos. Chem. Phys.* **2021**, *21*, 13099–13117. [CrossRef]
10. Turner, D.D.; Vogelmann, A.M.; Austin, R.T.; Barnard, J.C.; Cady-Pereira, K.; Chiu, J.C.; Clough, S.A.; Flynn, C.; Khaiyer, M.M.; Liljegren, J.; et al. Thin Liquid Water Clouds: Their Importance and Our Challenge. *Bull. Am. Meteorol. Soc.* **2007**, *88*, 177–190. [CrossRef]
11. Guy, H.; Brooks, I.M.; Turner, D.D.; Cox, C.J.; Rowe, P.M.; Shupe, M.D.; Walden, V.P.; Neely, R.R. Observations of Fog-Aerosol Interactions Over Central Greenland. *J. Geophys. Res. Atmos.* **2023**, *128*, e2023JD038718. [CrossRef]
12. Nurowska, K.; Mohammadi, M.; Malinowski, S.; Markowicz, K. Applicability of the low-cost OPC-N3 optical particle counter for microphysical measurements of fog. *Atmos. Meas. Tech.* **2023**, *16*, 2415–2430. [CrossRef]
13. Mazoyer, M.; Burnet, F.; Denjean, C. Experimental study on the evolution of droplet size distribution during the fog life cycle. *Atmos. Chem. Phys.* **2022**, *22*, 11305–11321. [CrossRef]
14. Cadeddu, M.P.; Liljegren, J.C.; Turner, D.D. The Atmospheric radiation measurement (ARM) program network of microwave radiometers: Instrumentation, data, and retrievals. *Atmos. Meas. Tech.* **2013**, *6*, 2359–2372. [CrossRef]

15. Marchand, R.; Ackerman, T.; Westwater, E.R.; Clough, S.A.; Cady-Pereira, K.; Liljegren, J.C. An assessment of microwave absorption models and retrievals of cloud liquid water using clear-sky data. *J. Geophys. Res. Atmos.* **2003**, *108*. [CrossRef]
16. Temimi, M.; Fonseca, R.M.; Nelli, N.R.; Valappil, V.K.; Weston, M.J.; Thota, M.S.; Wehbe, Y.; Yousef, L. On the analysis of ground-based microwave radiometer data during fog conditions. *Atmos. Res.* **2020**, *231*, 104652. [CrossRef]
17. Turner, D.D.; Löhnert, U. Ground-based temperature and humidity profiling: Combining active and passive remote sensors. *Atmos. Meas. Tech.* **2021**, *14*, 3033–3048. [CrossRef]
18. Marke, T.; Ebell, K.; Löhnert, U.; Turner, D.D. Statistical retrieval of thin liquid cloud microphysical properties using ground-based infrared and microwave observations. *J. Geophys. Res. Atmos.* **2016**, *121*, 14,558–14.573. [CrossRef]
19. Guy, H.; Turner, D.D.; Walden, V.P.; Brooks, I.M.; Neely, R.R. Passive Ground-Based Remote Sensing of Radiation Fog. *Atmos. Meas. Tech.* **2022**, *15*, 5095–5115. [CrossRef]
20. Chaurasia, S.; Sathiyamoorthy, V.; Paul Shukla, B.; Simon, B.; Joshi, P.C.; Pal, P.K. Night time fog detection using MODIS data over Northern India. *Meteorol. Appl.* **2011**, *18*, 483–494. [CrossRef]
21. Cermak, J.; Bendix, J. Detecting ground fog from space—A microphysics-based approach. *Int. J. Remote Sens.* **2011**, *32*, 3345–3371. [CrossRef]
22. Niu, J.; Yang, P.; Huang, H.L.; Davies, J.E.; Li, J.; Baum, B.A.; Hu, Y.X. A fast infrared radiative transfer model for overlapping clouds. *J. Quant. Spectrosc. Radiat. Transf.* **2007**, *103*, 447–459. [CrossRef]
23. Sieron, S.B.; Clothiaux, E.E.; Zhang, F.; Lu, Y.; Otkin, J.A. Comparison of using distribution-specific versus effective radius methods for hydrometeor single-scattering properties for all-sky microwave satellite radiance simulations with different microphysics parameterization schemes. *J. Geophys. Res. Atmos.* **2017**, *122*, 7027–7046. [CrossRef]
24. Jahani, B.; Cermak, J.; Andersen, H. Algorithm for continual monitoring of fog based on geostationary satellite imagery. *Atmos. Meas. Tech.* **2025**, *18*, 1927–1945. [CrossRef]
25. Nelli, N.; Francis, D.; Cherif, C.; Fonseca, R.; Ghedira, H. Automated night-time fog detection and masking using machine learning from near real-time satellite observations. *Sci. Remote Sens.* **2025**, *12*, 100297. [CrossRef]
26. Egli, S.; Thies, B.; Bendix, J. A Hybrid Approach for Fog Retrieval Based on a Combination of Satellite and Ground Truth Data. *Remote Sens.* **2018**, *10*, 628. [CrossRef]
27. Egli, S.; Thies, B.; Drews, R.; Cermak, J.; Bendix, J. A 10 year fog and low stratus climatology for Europe based on Meteosat Second Generation data. *Q. J. R. Meteorol. Soc.* **2019**, *145*, 1231–1244. [CrossRef]
28. Pauli, E.; Cermak, J.; Andersen, H. A satellite-based climatology of fog and low stratus formation and dissipation times in central Europe. *Q. J. R. Meteorol. Soc.* **2022**, *148*, 1439–1454. [CrossRef]
29. Zawadzka-Manko, O.; Markowicz, K.M. Long-Term Variability of Fog in Poland. *Int. J. Climatol.* **2025**, *45*, e8784. [CrossRef]
30. Curry, J.A.; Hobbs, P.V.; King, M.D.; Randall, D.A.; Minnis, P.; Isaac, G.A.; Pinto, J.O.; Uttal, T.; Bucholtz, A.; Cripe, D.G.; et al. FIRE Arctic Clouds Experiment. *Bull. Am. Meteorol. Soc.* **2000**, *81*, 5–30. [CrossRef]
31. Dong, X.; Xi, B.; Qiu, S.; Minnis, P.; Sun-Mack, S.; Rose, F. A radiation closure study of Arctic stratus cloud microphysical properties using the collocated satellite-surface data and Fu-Liou radiative transfer model. *J. Geophys. Res. Atmos.* **2016**, *121*, 10175–10198. [CrossRef]
32. Fu, Q.; Liou, K.N. On the Correlated *k*-Distribution Method for Radiative Transfer in Nonhomogeneous Atmospheres. *J. Atmos. Sci.* **1992**, *49*, 2139–2156. [CrossRef]
33. Fu, Q.; Liou, K.N. Parameterization of the Radiative Properties of Cirrus Clouds. *J. Atmos. Sci.* **1993**, *50*, 2008–2025. [CrossRef]
34. Rodgers, C.D. *Inverse Methods for Atmospheric Sounding: Theory and Practice*; World Scientific: Singapore, 2000. [CrossRef]
35. Nurowska, K. Microphysical and Optical Data of Radiation Fog in Strzyżów Valley, Poland. Dataset, Dane Badawcze UW (University of Warsaw Research Data Repository), V1. 2025. Available online: https://danebadawcze.uw.edu.pl/dataset.xhtml?persistentId=doi:10.58132/WPKQNT (accessed on 8 August 2025).
36. Nurowska, K.; Makuch, P.; Markowicz, K.M. Measurement report: Microphysical and optical characteristics of radiation fog—A study using in situ, remote sensing, and balloon techniques. *Atmos. Chem. Phys.* **2025**, *25*, 13493–13525. [CrossRef]
37. Holben, B.N.; Eck, T.F.; Slutsker, I.; Tanré, D.; Buis, J.P.; Setzer, A.; Vermote, E.; Reagan, J.A.; Kaufman, Y.J.; Nakajima, T.; et al. AERONET—A federated instrument network and data archive for aerosol characterization. *Remote Sens. Environ.* **1998**, *66*, 1–16. [CrossRef]
38. Giles, D.M.; Sinyuk, A.; Sorokin, M.G.; Schafer, J.S.; Smirnov, A.; Slutsker, I.; Eck, T.F.; Holben, B.N.; Lewis, J.R.; Campbell, J.R.; et al. AERONET Version 3 processing and all points quality assurance. *Atmos. Meas. Tech.* **2019**, *12*, 169–209. [CrossRef]
39. Copernicus Climate Change Service. ERA5 Hourly Data on Pressure Levels from 1940 to Present, 2023. Available online: https://cds.climate.copernicus.eu/datasets/reanalysis-era5-pressure-levels?tab=overview (accessed on 16 April 2026).
40. Klein, C.; Dabas, A. Relationship between optical extinction and liquid water content in fogs. *Atmos. Meas. Tech.* **2014**, *7*, 1277–1287. [CrossRef]
41. Podzimek, J. Droplet concentration and size distribution in haze and fog. *Stud. Geophys. Geod.* **1997**, *41*, 277–296. [CrossRef]

42. Kipp & Zonen. *CMP21, CMP22, SMP22—Pyranometer Datasheet*; Document ID ME-KZ-RE-ds-CMP21-CMP22-SMP22-EN-231023; Kipp & Zonen/OTT HydroMet: Delft, The Netherlands; Kempten, Germany, 2023.
43. *CNR4 Net Radiometer Instruction Manual*, revision 9/13; Campbell Scientific, Inc.: Logan, UT, USA, 2013.
44. Kipp & Zonen. *Net Radiometers (NR Lite2, CNR 4) Brochure*; Document ID 4414391-V2104; Kipp & Zonen: Delft, The Netherlands; OTT HydroMet: Kempten, Germany, 2021.
45. World Meteorological Organization. *Guide to Instruments and Methods of Observation*; Technical Report WMO-No. 8; World Meteorological Organization: Geneva, Switzerland, 2018.
46. *JCGM 100:2008*; Evaluation of Measurement Data—Guide to the Expression of Uncertainty in Measurement. GUM 1995 with minor corrections; JCGM (Joint Committee for Guides in Metrology): Sèvres, France, 2008.
47. Philipona, R.; Dutton, E.G.; Stoffel, T.; Michalsky, J.; Reda, I.; Stifter, A.; Wendling, P.; Wood, N.; Clough, S.A.; Mlawer, E.J.; et al. Atmospheric longwave irradiance uncertainty: Pyrgeometers compared to an absolute sky-scanning radiometer, atmospheric emitted radiance interferometer, and radiative transfer model calculations. *J. Geophys. Res. Atmos.* **2001**, *106*, 28129–28141. [CrossRef]
48. Vuilleumier, L.; Hauser, M.; Félix, C.; Vignola, F.; Blanc, P.; Kazantzidis, A.; Calpini, B. Accuracy of ground surface broadband shortwave radiation monitoring. *J. Geophys. Res. Atmos.* **2014**, *119*, 13838–13860. [CrossRef]
49. Stoffel, T. *Precision Infrared Radiometer (Pyrgeometer) Handbook*; Technical Report ARM TR-023; U.S. Department of Energy, Atmospheric Radiation Measurement Program: Washington, DC, USA, 2004.
50. Stephens, G.L. Radiation Profiles in Extended Water Clouds. I: Theory. *J. Atmos. Sci.* **1978**, *35*, 2111–2122. [CrossRef]
51. Stephens, G.L. Radiation Profiles in Extended Water Clouds. II: Parameterization Schemes. *J. Atmos. Sci.* **1978**, *35*, 2123–2132. [CrossRef]
52. Deirmendjian, D. *Electromagnetic Scattering on Spherical Polydispersions*; Elsevier Scientific Publishing: New York, NY, USA, 1969; p. 290.
53. Roach, W.T.; Brown, R.; Caughey, S.J.; Garland, J.A.; Readings, C.J. The physics of radiation fog: I—A field study. *Q. J. R. Meteorol. Soc.* **1976**, *102*, 313–333. [CrossRef]
54. Duynkerke, P.G. Radiation fog: A comparison of model simulation with detailed observations. *Mon. Weather Rev.* **1991**, *119*, 324–341. [CrossRef]
55. Wærsted, E.G.; Haeffelin, M.; Dupont, J.C.; Delanoë, J.; Dubuisson, P. Radiation in fog: Quantification of the impact on fog liquid water based on ground-based remote sensing. *Atmos. Chem. Phys.* **2017**, *17*, 10811–10835. [CrossRef]
56. Haeffelin, M.; Bergot, T.; Elias, T.; Tardif, R.; Carrer, D.; Chazette, P.; Colomb, M.; Drobinski, P.; Dupont, E.; Dupont, J.C.; et al. PARISFOG: Shedding new light on fog physical processes. *Bull. Am. Meteorol. Soc.* **2010**, *91*, 767–783. [CrossRef]
57. Bergot, T.; Guedalia, D. Numerical forecasting of radiation fog. Part I: Numerical model and sensitivity tests. *Mon. Weather Rev.* **1994**, *122*, 1218–1230. [CrossRef]
58. Price, J. Radiation fog. Part I: Observations of stability and drop size distributions. *Bound.-Layer Meteorol.* **2011**, *139*, 167–191. [CrossRef]
59. Bell, A.; Martinet, P.; Caumont, O.; Burnet, F.; Delanoë, J.; Jorquera, S.; Seity, Y.; Unger, V. An optimal estimation algorithm for the retrieval of fog and low cloud thermodynamic and micro-physical properties. *Atmos. Meas. Tech.* **2022**, *15*, 5415–5438. [CrossRef]

Disclaimer/Publisher's Note: The statements, opinions and data contained in all publications are solely those of the individual author(s) and contributor(s) and not of MDPI and/or the editor(s). MDPI and/or the editor(s) disclaim responsibility for any injury to people or property resulting from any ideas, methods, instructions or products referred to in the content.